UNIVERSITY OF CANTERBURY

MASTERS THESIS

Modelling of Bubble Nucleation and Growth in a Combusting Metal Droplet

---

Author:
Andrew Lange

Supervisor:
Prof. Mathieu Sellier

A thesis submitted in fulfillment of the requirements for the degree of Master of Engineering

in the

Department of Mechanical Engineering

April 16, 2021

Abstract

Numerous applications are interested in the use of combusting metal powders such as explosives, propellants, pyrotechnics, and bio-agent defeat. Optimising the performance of these reactions is of great interest to many of these fields. Particles of such powders have been observed to explode during combustion, yielding new surface areas and potentially enhancing the burn rate of the powder. It is thought that better understanding this process will help to design more optimised powders with greater benefits. Following the work in Wainwright et al. (2019), this thesis investigates the bubble growth within combusting metal droplets and compares the data from experimental recordings with solutions of a mathematical model. This model is developed from the Navier-Stokes equations in spherical coordinates and by applying assumptions and substituting expressions of mass continuity is simplified to coupled first order ordinary differential equations. These simplifications allow the equations to be solved using ode45 in MATLAB to obtain a plot of the bubble radius over time.

A number of candidate functions for expressing the molar flow of gas into the bubble are generated for use in the model. The graphs for different functions for molar flow rate are compared to radius data measured from images of bubble growth events from experiments done by Wainwright et al. of a combusting aluminium and zirconium alloy powder. Within the limits of uncertainty there is most agreement between the model solution and experimental data when the flow of nitrogen into the bubble is linearly proportional to the bubble radius. This finding should help shed light on the mass transfer process during bubble growth.

Modelling of the bubble expansion was also completed using COMSOL Multiphysics for a two-dimensional axisymmetric case. This approach enables the influence of nucleation position to be evaluated. When concentric, the solution has a similar profile to that obtained from the ODE which gives confidence in the validity of the off-centre bubble simulations. It was found that as the location of the bubble nucleation site gets closer to the surface of the droplet, there is no large change in the growth rate of the bubble. The closer the nucleation is to the droplet surface does impact the rate at which the liquid phase thins as there does not appear to be flow in the liquid phase around the bubble, and then results in longer calculation times due to the warping mesh. As the liquid phase thins, the likelihood of the surface rupturing for some instability increases and so off-centre nucleations would then result in surface bursting at a smaller bubble size than concentric nucleation, however without the entire droplet breaking apart.

Further investigation towards understanding the different transport mechanisms was made by modelling chemical transport from diffusion and adsorption. To this

end, the diffusion equation was applied to the domain with a coordinate transform and coupled with the bubble growth ODE. This PDE was then solved with the Crank-Nicolson method and flux was input to the ODE to calculate the growth of the bubble. Different boundary conditions were applied to the domain with Dirchlet, Neumann, and Robin conditions solved and compared with data from the event analysis. Flux into the bubble for the Dirichlet and Robin conditions was calculated from the concentration profile at the given time step. The resulting bubble radius profile did not agree with the experimental data for these conditions. The Neumann condition showed the concentration plots for molar flow that matches the data. The required initial concentration for the simulation leads to an estimated initial amount of 3.5332×10^{-12} mol of nitrogen in the liquid phase. Compared with the amount of metal atoms in solution, this makes up roughly 0.3% of the atomic matter which suggests that the required initial concentration is attainable for most particles to undergo bubble growth.

Acknowledgements

I would first like to thank my supervisors Mathieu Sellier and James Hewett for guiding and supporting me in the pursuit of this work, and in particular Mathieu for providing me the opportunity to undertake academic research in a field that I find most interesting. Courses of his I took in undergraduate studies were the key factor in choosing the area for me to pursue studies in, and being able to go back and tutor those same courses has been a pleasure.

Many thanks to Tim Weihs, Elliot Wainwright, and all the faculty at Johns Hopkins University for giving me this research topic and funding my studies. I am truly grateful for your contributions towards my financial ability to perform research and in collaborating on this particular case. Your feedback has been immensely helpful in increasing my understanding in materials science, and so once again thank you.

Cheers to my fellow postgraduate students for making the postgrad office such an enjoyable space to be a part of. Also thank you to all those who helped when I was stuck with something and for sharing knowledge.

Lastly, I would like to thank my parents Sherideen and Tony for encouraging and supporting me through my journey towards higher study. While it may not always be obvious I do very much appreciate that you are always there for me, even when I don't think I need it. I would also like to mention my brother Austin, so that he does not feel left out and to thank him for his friendship.

Contents

Abstract **iii**

Acknowledgements **v**

1 Introduction **1**
1.1 Microexplosion and Combustion 2
1.2 Dynamics Modelling of Encapsulated Bubble Growth 2
1.3 Surface Tension 5
1.4 Surface Bursting 6

2 Mathematical Model **7**
2.1 Assumptions 7
2.2 Physical System 7
2.3 Equations 9
2.4 Numerical Methods 11
2.5 Parameter Sensitivity 17

3 Bubble Growth Event Analysis **23**
3.1 Introduction 23
3.2 Methods 23
3.3 Results & Discussion 26
3.4 Conclusions 30

4 Multidimensional Simulation **33**
4.1 Introduction 33
4.2 Method 35
4.3 Results & Discussion 41
4.3.1 ODE Comparisons 41
4.3.2 Off-Centre Nucleation 44
4.4 Conclusion 48

5 Interfacial and Diffusive Transport **51**
5.1 Introduction 51
5.2 Methods 51
5.3 Results & Discussion 57
5.4 Conclusion 63

6 Conclusions **65**

List of Figures

1.1 Different modes of bubble growth in the metal droplet (Wainwright et al., 2019) . . . 3
1.2 Plot of bubble growth rate against initial droplet size (Wainwright et al., 2019) . . . 3

2.1 Physical model of the bubble growth within the droplet. . . . 8
2.2 Schematic of the forces acting on the bubble and droplet interfaces with viscous forces, surface tension, and pressure. . . . 8
2.3 Comparison of different ODE solvers in MATLAB R2018b using parameters from Event 1 for zero-th order radius molar flow rate. . . . 14
2.4 Comparison of different ODE solvers in MATLAB R2018b using parameters from Event 1 for first order radius molar flow rate. . . . 15
2.5 Comparison of different ODE solvers in MATLAB R2018b using parameters from Event 1 for second order radius molar flow rate. . . . 16
2.6 Parameter sensitivity plots for molar flow rate with zero-th order radius 18
2.7 Parameter sensitivity plots for molar flow rate with first order radius . 19
2.8 Parameter sensitivity plots for molar flow rate with second order radius 20

3.1 Still photo of Al:Zr powder combustion from x-ray phase contrast imaging from Wainwright et al. (2019). The particle to be measured is outlined with a square box. . . . 24
3.2 Unprocessed image from Figure 3.1 cropped to focus on particle for measuring. The full line shows the measured area of the bubble in Fiji using the circle tool. The dashed lines show the increased and reduced measurements for determining the uncertainty bound. . . . 25
3.3 Bubble growth model for Event 1 solved by `ode45`. . . . 28
3.4 Bubble growth model for Event 2 solved by `ode45`. . . . 29
3.5 Bubble growth model for Event 3 solved by `ode45`. . . . 30
3.6 Bubble growth model for Event 1 solved by `ode45` for changes of value 10% higher and lower for different parameters. . . . 31

4.1 Image of geometry for representing the bubble-droplet system . . . 36
4.2 Images of the mesh used for calculating the system of equations. The top image shows the mesh over the full geometry while the bottom image zooms in to the bubble domain to show the boundaries in detail. 38

4.3 Plots of bubble radius, growth rate, and pressure from ODE simulation to obtain consistent initial values for COMSOL. 39
4.4 Diagram showing key dimensions for tracking evolution of the system as the bubble expands. 40
4.5 Surface plots of velocity magnitude for concentric bubble growth at times of 1 µs, 10 µs, 50 µs, and 100 µs respectively. 42
4.6 Plot of the probed droplet radius compared with that calculated from conservation of mass 43
4.7 Plot of radius over time from COMSOL compared with ode15s for concentric cases with different initial conditions. 43
4.8 Plot of pressure over time from COMSOL compared with ode15s for concentric cases with different starting radii 44
4.9 Surface plots of velocity magnitude at 100 µs for initial offsets of ζ equal to 0.0, 0.1, 0.2, and 0.3 respectively 45
4.10 Plot of bubble radius over time from COMSOL for different initial offsets 46
4.11 Plots of mesh quality at 100 µs for initial offsets of ζ equal to 0, 0.1, 0.2, and 0.3 respectively 47
4.12 Plots of the ratio of distance between bubble and droplet centres to initial droplet radius 47
4.13 Plots of the ratio of thickness of the liquid phase between the thickest and thinnest sections. 48

5.1 Spatial domain of liquid phase for solving Fick's Second Law with boundary conditions 52
5.2 Bubble radius profile for the Neumann boundary condition compared to data from Event 1. 57
5.3 Concentration profiles for the Neumann boundary condition over time. 58
5.4 Bubble radius profile for the Dirichlet boundary condition compared to data from Event 1. 59
5.5 Concentration profiles for the Dirichlet boundary condition over time. 59
5.6 Bubble radius profile for the Dirichlet boundary condition compared to data from Event 1 with increased diffusion and less initial concentration. 60
5.7 Concentration profiles for the Dirichlet boundary condition over time with increased diffusion and less initial concentration. 61
5.8 Bubble radius profile for the Robin boundary condition compared to data from Event 1. 61
5.9 Concentration profiles for the Robin boundary condition over time. . . 62

Chapter 1

Introduction

Metal powders are commonly burned as an additive material in explosives, propellants, pyrotechnics, and bio-agent defeat formulations. During the combustion process, some metallic powders form bubbles inside the molten droplet. If the bubble grows quickly it can cause the droplet to fragment in a process known as a microexplosion. It is theorised that by selecting materials with a propensity for microexplosions and combining them with other metals with beneficial combustions reactions, a composite will have formed that has better combustion from enhanced secondary atomisation. This is due to the bursting droplets revealing fresh surfaces of metal for further reactions while retaining the energetic reaction that makes it suitable for the previously mentioned applications. Having a good secondary burn rate also allows for a coarser powder which can help in applications where the powder needs to be thrown or dropped some distance before being ignited and combusting. The aim of this project is to model the nucleation and expansion of a gas bubble inside the molten droplet of metal undergoing combustion to better understand the mechanics of bubble growth that leads to microexplosion and how they relate to the properties of the metal. One goal of this project is to match the simulated bubble growth process to the videos recorded by Wainwright et al. (2019) in their experiment phenomenologically to estimate the properties of surface tension and viscosity for the molten composite particle of Al:Zr. This process is required as calculating the properties of surface tension and viscosity for composite metal alloys is typically only done in experiments as impurities and temperature dependence make attempts to calculate them using atomic forces imprecise, especially for a composite metal solution. As a result of the temperature dependence, there is currently no reasonable data for the metals in this process as typical methods of measurement are unable to be employed at temperatures of 2800K such as in this application. Another goal is to try and determine at what point in the bubble expansion the droplet splits apart. This would let the model identify what material properties directly influence microexplosions and predict when the droplet would explode given the initial conditions. To achieve these goals a range of models were created and validated by comparing the results obtained to those given by commercial software packages. In each case the results were also tested for convergence and mesh independence. The models progressively

get more complex as assumptions about the bubble expansion and combustion are stripped away. This reveals what parts of the reaction have the largest impact on microexplosions.

1.1 Microexplosion and Combustion

During the combustion of highly energetic metal powders, bubbles may nucleate within the molten droplet and expand, potentially causing the droplet to fragment in a process termed a microexplosion. Studies have been done on a representative composite powder of Al:Zr with a 1:1 atomic ratio to view the nucleation and explosion processes (Wainwright et al. (2018), Wainwright et al. (2019)). In these studies, they propose that the bubbles nucleate and grow as a result of nitrogen being displaced by oxygen as it oxidises the zirconium in the condensed state. This process occurs after enough aluminium has evaporated from the particle in the two-stage reaction. This nitrogen gas is absorbed into the solution in the first stage of the reaction and upon being displaced by oxygen attaches to impurities inside the particle. The nucleation sites are theorised to be oxide or nitride precipitates of Zr or Hf impurities with high melting points and their location is thought to influence the microexplosion behaviour. Another factor that alters how the particle reacts is the rate of bubble growth. The combination of different rates with the location of the bubble determine the mode of bubbling within the droplet. With slow growth rates and central nucleation, the droplet will form a hollow shell, while fast growth rates will lead to microexplosions. If the bubble nucleates close to the edge of the droplet it will repeatedly bubble with gas jetting from the surface for moderate or high bubble growth rates. Wainwright et al. suggest that the growth rate depends mostly on the concentration of N_2 in the solution, with higher growth rates correlating to higher concentrations. The different modes with their associated criteria are thus shown in Figure 1.1 and Figure 1.2 shows growth rates for multiple particles with their respective modes of bubble growth.

1.2 Dynamics Modelling of Encapsulated Bubble Growth

Liu et al. (2017) model the bubble growth process in a superheated water droplet due to rapid depressurisation. They derive a numerical model from the conservation of momentum equation in spherical coordinates by substituting in an expression of radial velocity in terms of the bubble radius rate of change. From there, the equation is integrated from the bubble surface to the droplet surface and expressions resulting

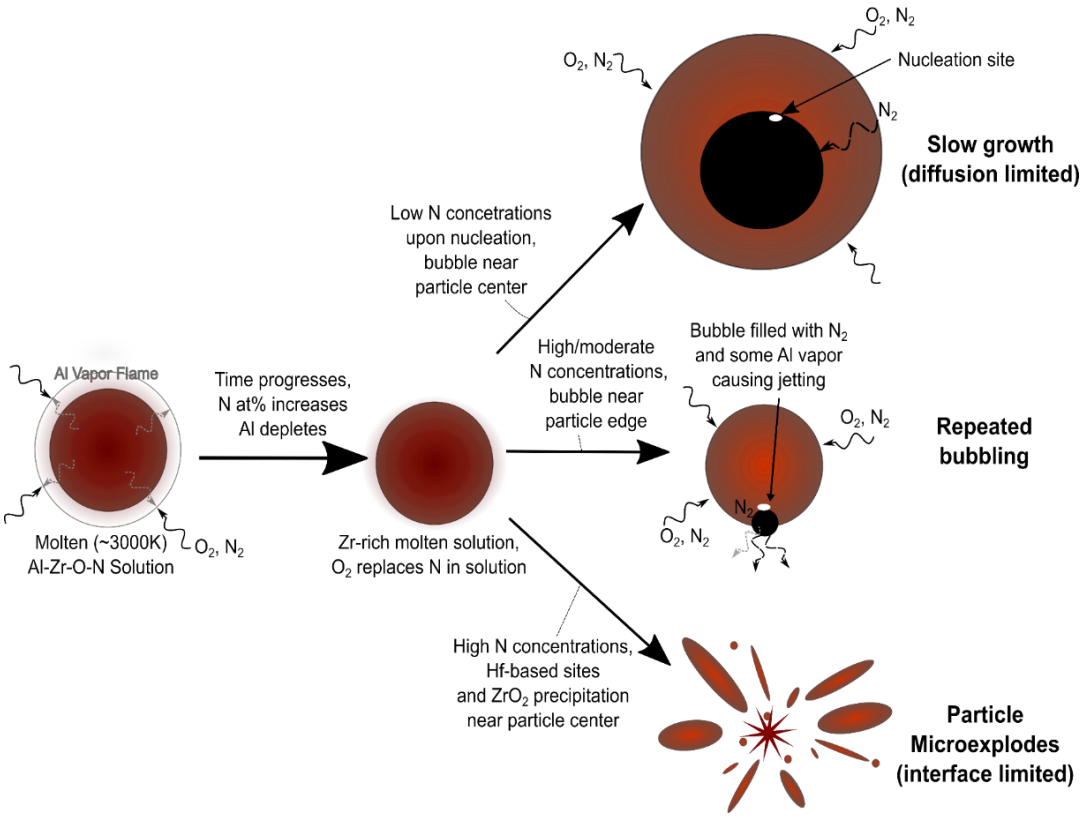

FIGURE 1.1: Different modes of bubble growth in the metal droplet (Wainwright et al., 2019)

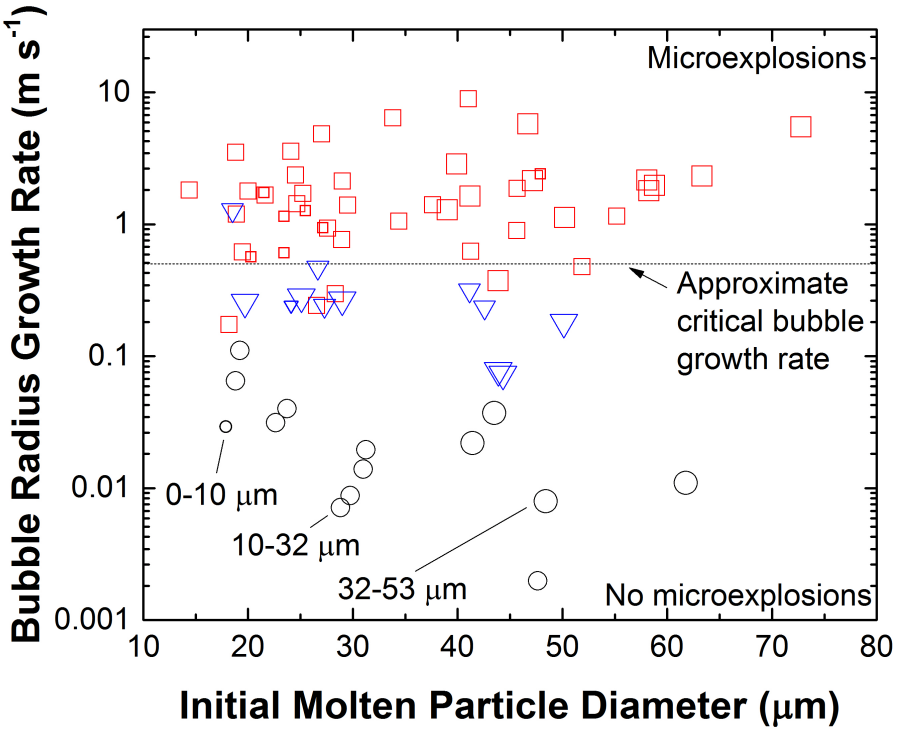

FIGURE 1.2: Plot of bubble growth rate against initial droplet size (Wainwright et al., 2019)

from a force balance from the interfaces are substituted in giving the equation

$$\left(r_B - \frac{{r_B}^2}{r_D}\right)\frac{d^2 r_B}{dt^2} + \left(\frac{3}{2} - \frac{2r_B}{r_D} + \frac{{r_B}^4}{2{r_D}^4}\right)\left(\frac{dr_B}{dt}\right)^2 = \frac{1}{\rho_l}\left(P_g - P_\infty - \frac{2\sigma_l}{r_B} - \frac{2\sigma_l}{r_D} - \left(\frac{4\mu_l}{r_B} - \frac{4\mu_l {r_B}^2}{{r_D}^3}\right)\frac{dr_B}{dt}\right) \quad (1.1)$$

Where r_B is the bubble radius; r_D is the radius of the droplet; P_g is the pressure of the gas at the bubble interface; P_∞ is the ambient pressure; ρ_l and μ_l are the density and viscosity of the liquid phase respectively; and σ_l is the interfacial or surface tension of the liquid which is the same at both the droplet and the bubble surfaces. This equation takes the same form as the classical Rayleigh-Plesset equation when taking the limit with $r_D \to \infty$. As this is a one-dimensional ordinary differential equation, it can be solved using the Runge-Kutta method, decomposed into two first order differential equations.

Feng and Bertelo (2004) study the nucleation and growth of bubbles in a polymer foam as a heterogeneous model based on diffusion of gasses into microvoids on solid particles. They calculate the nucleation rate from some bubble detachment time until some critical radius and from there consider the viscoelastic stresses in the polymer to model the bubble growth. This provides a solution method for non-Newtonian materials. It also features a mass balance across the bubble interface using expressions for diffusion across the boundary.

Xia and Shinjo (2017), as well as Shinjo et al. (2014) and Shinjo et al. (2016) examine the dynamics of microexplosion and puffing in an emulsion fuel droplet. In these papers they simulate the break-up of the parent fuel particle due to explosive boiling of the water sub-droplet. The investigation was conducted using high fidelity numerical solutions with results that agree with the experimental observations in Wainwright et al. (2019) for droplet break up processes at different locations, despite the differences in materials and processes. From there they continue to investigate the dynamics in the fuel droplet under the influence of convective heating and propose a model to approximate the temperature distribution inside the droplet.

Sazhin et al. (2019) also submit a model for puffing/microexplosions in emulsion fuel droplets. Their approach is much simpler than the model used by Shinjo et al. (2016) and assumes that the fuel and water droplets are concentric and spherical. Within the paper they derive the conduction of heat through the fuel phase assuming a constant temperature at the surface of the fuel droplet with the Dirichlet boundary condition. Despite the simplification, the model is found to describe the time until puffing occurs, although contains a tendency to underestimate the time compared to experimental data. Due to the method of derivation, it may be generalised to allow for analysis of the combusting metal droplet easily.

Kirk and Gunter (1970) analyse the pressure distribution in a journal bearing using numerical integration of the pressure equation, derived from the Navier-Stokes equations to form the Reynolds equation for the bearing based on a short bearing assumption. They then derive the equations of motion for the movement of the bearing to determine an expression for the force in the bearing with respect to time. This solution method could be implemented in modelling the movement of off-centre bubbles within the droplet as it is theorised that the bubbles migrate inward due to some induced pressure profile on the bubble as a result of its expansion.

1.3 Surface Tension

Surface tension is a property of free deformable surfaces such as those in fluids. It is caused by surface atoms having higher energy than bulk atoms, and so the system tries to minimise the free energy by having as few surface atoms as possible. This results in a net force opposing deformation of the surface related to the bond energy of the atoms. This is what causes droplets and bubbles to hold their shape and also resists the bubble expansion. It is therefore an important property in modelling the combusting droplet system.

There is significant difficulty in obtaining accurate values of surface tension in liquid metals due to highly reactive surfaces and high temperatures. Egry et al. (2010) reviewed the modern methods for determining surface tension in liquid metals. They compare experimental methods involving the formation of a droplet and thermodynamic methods that calculate the sum of bond energies in the surface. For the combusting system, it is unlikely that any of the methods proposed would be able to accurately predict surface tension in the composite due to the variance in atoms, high temperatures, and reactivity of the surface.

Mills and Su (2006) assessed a large range of results from researchers for multiple different metals and give recommended values as a function of temperature. Most experiments performed cover a large range of temperatures that near the boiling point of aluminium that the droplet experiences during combustion. It is seen that temperature has an approximately linear correlation with surface tension and so the value for pure metals at higher temperatures can be calculated using formulas provided in the paper. These equations do not take into account the influence of oxygen atoms reducing the surface tension in the droplets, which can vary wildly from experiment to experiment, nor does it give a way to resolve surface tension in a composite solution. A simplistic approach would be to average the values of surface tension for the two metals as calculated by the equations proposed as a starting point for the model. With enough resolution in the numerical solution it may be possible for the model to match recordings of microexplosion or bubble growth from experiments and be able to infer values of surface tension in physical droplets.

1.4 Surface Bursting

One of the aims of this project is to understand how the properties of the metals in the droplet contribute to microexplosions. In the previous sections the dynamics of bubble growth are examined and so the next step is to investigate the physics behind how the bubble expansion causes the droplet to burst.

Bremond and Villermaux (2005) explores the reaction of a thin film of liquid to a pressure wave. An impulsive Rayleigh Taylor instability is found to predict the mode selection and time of growth for the break-up of the film into droplets. This analysis provides a criterion for the film bursting time and hole density that could be adapted for the combusting droplet.

Wang et al. (2015) models the bursting of a large bubble at a free surface using the boundary integral method. Their numerical model is then validated by experiments that show qualitative agreement between results. Complexity arises in resolving the free surface boundary as the bubble interface approaches it. To resolve this in the model, Wang et al. (2015) perform a numerical cut when some minimum distance between the surfaces is reached, thus joining the bubble together with the free surface of the liquid. This approach may be feasible when the bubble nucleates close to the surface of the droplet but is unlikely to work for central nucleation.

Barthès-Biesel and Acrivos (1973) present a model for predicting the deformation and burst of a liquid droplet suspended freely in a linear shear field. For this, they expand the solution for the creeping flow equations and use linear stability theory to determine the onset of bursting. The criterion for droplet bursting is found to confirm Taylor's hypothesis that droplet breakup occurs when the viscous forces exceed the surface tension when the deformation in the droplet is higher than some critical value.

Chapter 2

Mathematical Model

2.1 Assumptions

To model the bubble growth inside the molten droplet the following assumptions were made: (1) there is one bubble inside the droplet; (2) the bubble and the droplet are both spherical and concentric, and that bubble growth is radially symmetric; (3) the bubble begins growing from some initial critical radius; (4) temperature is constant throughout the bubble and droplet; (5) the bubble is filled only with nitrogen and it behaves like an ideal gas; (6) the liquid phase consists of a molten Al:Zr:O:N solution which is incompressible and has a much larger density than the gas phase; (7) the outer interface of the droplet is only interacting with the atmosphere, any vapour or oxide phases that may affect growth of the bubble are ignored; (8) the bubble grows due to some molar flux of nitrogen out of the liquid phase into the bubble with no other mass transfer across any other interfaces; (9) change of mass in the droplet from Al-vaporisation is negligible and no other matter is leaving the system; (10) surface tension and viscosity of the liquid phase are only dependent on temperature and are therefore constant following assumption (4).

2.2 Physical System

With these assumptions present, the model of the system can be generated using an adaptation of the method used by Liu et al. (2017) for a super-heated water droplet. Illustrations of the physical domain are shown with Figure 2.1 displaying the whole system and Figure 2.2 showing the forces acting on the interfaces.

In these diagrams r_B is the bubble radius and r_D is the radius of the droplet surface which both change over the period of bubble growth. Fluid properties given by ρ_l, σ_l, μ_l, and T_l are the density, surface tension, dynamic viscosity and temperature of the liquid phase respectively. Other properties of P_B and T_B are the pressure and temperature in the bubble, while P_∞ and T_∞ are pressure and temperature of the surrounding air. With assumption (4) the temperatures of the liquid and gas phases

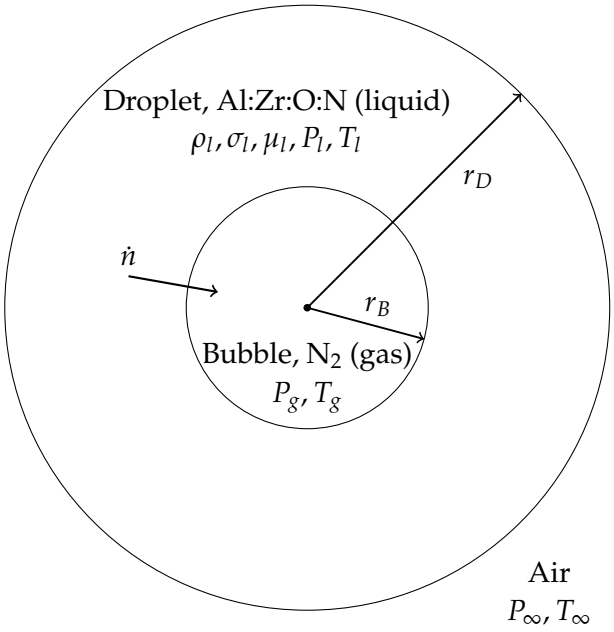

FIGURE 2.1: Physical model of the bubble growth within the droplet.

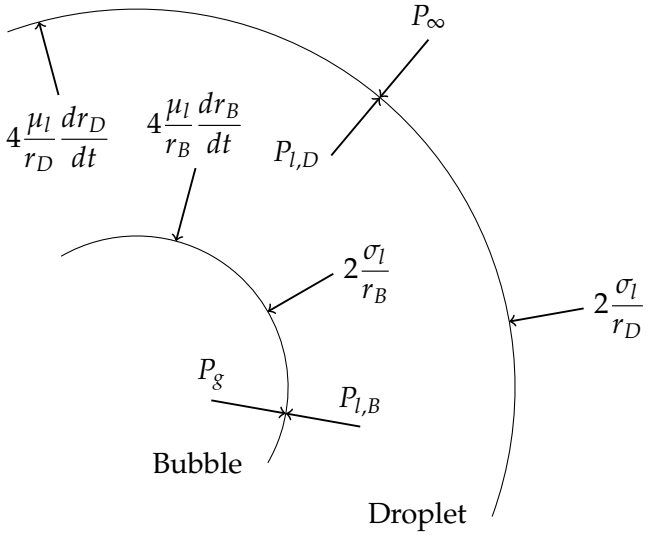

FIGURE 2.2: Schematic of the forces acting on the bubble and droplet interfaces with viscous forces, surface tension, and pressure.

are the same such that $T_l = T_g = T$. Additionally, $\dot{n}$ is the molar flow of gaseous nitrogen out of solution into the bubble, which drives the bubble growth represented as $\frac{dr_B}{dt}$. In the interfacial force schematic $P_{l,B}$ and $P_{l,D}$ are the pressures at the bubble and droplet surfaces in the liquid phase.

2.3 Equations

Balancing the forces on the interfaces at $r = r_B$ and $r = r_D$ then rearranging yields the expressions

$$P_{l,B} = P_g - 2\frac{\sigma_l}{r_B} - 4\frac{\mu_l}{r_B}\frac{dr_B}{dt} \tag{2.1}$$

$$P_{l,D} = P_\infty + 2\frac{\sigma_l}{r_D} - 4\frac{\mu_l}{r_D}\frac{dr_D}{dt} \tag{2.2}$$

Following assumption (2) that the bubble is concentric with growth being radially symmetric and ignoring the effect of gravity, the governing equation becomes the single r-component of the Navier-Stokes equations

$$\frac{\partial u}{\partial t} + u\frac{\partial u}{\partial r} = -\frac{1}{\rho_l}\frac{\partial P}{\partial r} + \frac{\mu_l}{\rho_l}\left(\frac{1}{r^2}\frac{\partial}{\partial r}\left(r^2\frac{\partial u}{\partial r}\right) - 2\frac{u}{r^2}\right) \tag{2.3}$$

And the mass continuity equation is

$$\frac{\rho_l}{r^2}\frac{\partial}{\partial r}\left(r^2 u\right) = 0 \tag{2.4}$$

Conservation of mass requires the radially outward velocity, $u(r,t)$, must be inversely proportional to the square of the distance from the bubble centre given by some function

$$u(r,t) = \frac{f(t)}{r^2} \tag{2.5}$$

With assumption (6) that the density of the liquid phase is much greater than that of the gaseous bubble, the velocity at the interface can be approximated with the case of zero mass transport across the interface

$$u(r_B,t) = \frac{dr_B}{dt} = \frac{f(t)}{{r_B}^2} \tag{2.6}$$

This then gives

$$f(t) = {r_B}^2\frac{dr_B}{dt} \tag{2.7}$$

which can then be substituted into Equation (2.5) to yield

$$u(r,t) = \frac{dr_B}{dt}\frac{{r_B}^2}{r^2} \tag{2.8}$$

This expression for the radial velocity is then substituted into Equation (2.3) and

integrated from the bubble surface at $r = r_B$, to the droplet surface at $r = r_D$. Following this integration $\frac{\partial P}{\partial r} = P_{l,D} - P_{l,B}$ and in substituting Equations (2.1) and (2.2) this yields a second order ordinary differential equation (ODE) for the bubble radius, r_B, as the dependent variable

$$\left(r_B - \frac{{r_B}^2}{r_D}\right)\frac{d^2 r_B}{dt^2} + \left(\frac{3}{2} - \frac{2r_B}{r_D} + \frac{{r_B}^4}{2{r_D}^4}\right)\left(\frac{dr_B}{dt}\right)^2 = \frac{1}{\rho_l}\left(P_g - P_\infty - \frac{2\sigma_l}{r_B} - \frac{2\sigma_l}{r_D} - \left(\frac{4\mu_l}{r_B} - \frac{4\mu_l {r_B}^2}{{r_D}^3}\right)\frac{dr_B}{dt}\right) \tag{2.9}$$

Assuming that the mass and density of the molten metal are relatively constant over the course of the bubble growth, an expression for the droplet radius in terms of the bubble radius can be substituted in

$$r_D = \sqrt[3]{{r_{D,0}}^3 + {r_B}^3} \tag{2.10}$$

Where $r_{D,0}$ is the initial droplet radius before the bubble begins growing.
By assuming that the nitrogen in the bubble behaves like an ideal gas, the pressure inside the bubble which drives the growth can be found using the ideal gas law.

$$P_g = \frac{nRT}{V} = \frac{3nRT}{4\pi {r_B}^3} \tag{2.11}$$

To determine the pressure in the bubble, the amount of moles of nitrogen must be known. This quantity is time dependent and can be calculated based on the rate of flow into the bubble using

$$n(t) = \int_0^t \dot{n} dt + n_0 \tag{2.12}$$

in which the rate of nitrogen entering the bubble, $\dot{n}$, may vary with time and can be expressed as

$$\dot{n}(t) = J_n A_B = J_n 4\pi {r_B}^2 \tag{2.13}$$

where J_n is the molar flux of nitrogen molecules into the bubble and A_B is the area of the bubble interface, calculated using the bubble radius. In this equation it is unclear how the flux may change over time. It is theorised that for interfacial controlled growth it might be constant over time, depending on how the average nitrogen concentration in the liquid phase progresses. If diffusion is the rate limiting process then flux would be large initially when the gradient of nitrogen concentration is highest before decreasing as the reaction progresses.

Failing to predict which mechanism is rate limiting means that multiple schemes are needed to evaluate the proportionality of the molar accumulation in the bubble. The

proposed scheme for comparing to data from experiments is

$$\int_0^t \dot{n}dt = \dot{N}_i {r_B}^{(i)} t, \qquad i = 0, 1, 2 \tag{2.14}$$

whereby $\dot{N}_i$ is a constant unknown value dependent on the order of bubble radius. This treatment lumps all the unknown time dependent terms into the geometry term. Evaluating Equation (2.12) with this expression substituted in gives

$$n_i(t) = \dot{N}_i {r_B}^{(i)} t + P_{g,0} \frac{4\pi {r_{B,0}}^3}{3RT}, \qquad i = 0, 1, 2 \tag{2.15}$$

in which the initial amount of moles at $t = 0$ has been substituted for a rearranged expression of the ideal gas law for some initial values of pressure and radius.

In the case where $i = 2$, the amount of nitrogen is proportional to radius squared. This would then imply that flux is constant as proposed for interfacial controlled growth. The other cases however indicate that flux would be inversely related to the bubble radius which may be the case for diffusion control or potentially the interface control depending on the progression and distribution of nitrogen concentration in the liquid phase.

2.4 Numerical Methods

There are a number of different numerical methods for solving ODEs such as Equation (2.9), the most notable of which can be found in Butcher (1987). For this equation, both the Runge-Kutta with Dormand-Prince coefficients (RKDP) as an explicit method and linear multistep with backwards differencing (BDF) as an implicit method were compared. As this is a second order non-linear equation, it first must be decomposed into a set of coupled first order ODEs

$$\frac{dr_B}{dt} = q \tag{2.16}$$

$$\frac{dq}{dt} = -\frac{\frac{3}{2} - \frac{2r_B}{r_D} + \frac{{r_B}^4}{2{r_D}^4}}{r_B - \frac{{r_B}^2}{r_D}} q^2 + \frac{P_g - P_\infty - \frac{2\sigma_l}{r_B} - \frac{2\sigma_l}{r_D} - \left(\frac{4\mu_l}{r_B} - \frac{4\mu_l {r_B}^2}{{r_D}^3}\right) q}{\rho_l \left(r_B - \frac{{r_B}^2}{r_D}\right)} \tag{2.17}$$

with q being some intermediate variable defined as the rate of change of the bubble radius. These equations are then expressed in a function vector such that

$$\mathbf{y} = \begin{bmatrix} r_B \\ q \end{bmatrix} \tag{2.18}$$

and then taking the time derivative gives

$$\mathbf{y}' = \mathbf{f}(t, \mathbf{y}) = \begin{bmatrix} f_1(t, \mathbf{y}) \\ f_2(t, \mathbf{y}) \end{bmatrix} = \begin{bmatrix} \frac{dr_B}{dt} \\ \frac{dq}{dt} \end{bmatrix} \tag{2.19}$$

where the entries of $\mathbf{f}(t, \mathbf{y})$ are Equations (2.16) and (2.17). Solving for the variables in $\mathbf{y}$ using a Runge-Kutta method can be expressed as

$$\mathbf{y}_{n+1} = \mathbf{y}_n + h \sum_{i=1}^{s} b_i \mathbf{k}_i \tag{2.20}$$

$$\mathbf{k}_i = \mathbf{f}(t_n + c_i h, \mathbf{y}_n + h \sum_{j=1}^{s} a_{i,j} \mathbf{k}_j) \tag{2.21}$$

$$t_{n+1} = t_n + h \tag{2.22}$$

where h is the step size, and $a_{i,j}$, b_i, and c_i are elements of the coefficient matrices $\mathbf{A}$, $\mathbf{b}$, and $\mathbf{c}$ as determined by the order of the chosen method with s number of stages. The matrices can be arranged in a compact form called a butcher tableau (Butcher, 1987) with the placement of

$\mathbf{c}$	$\mathbf{A}$
	$\mathbf{b}^\intercal$

When $\mathbf{A}$ is lower triangular such that $a_{i,j} = 0$ for all $j > i - 1$ the method is explicit as all steps of the solution depend only on steps that occurred before the current stage. If some $a_{i,j} \neq 0$ exists for any $j > i - 1$, then the method is said to implicit as it requires the use of Newton's method to evaluate the stages where $\mathbf{k}_i$ is a function of itself. Dormand-Prince is an explicit method with fourth- and fifth- order accuracy which can be implemented using MATLAB's inbuilt function ode45. The Butcher tableau of the coefficients is shown in Table 2.1. In this table, the first row of $\mathbf{b}^\intercal$ values gives the fifth-order accurate solution, while the second row provides an error estimate when subtracted from the first solution.

Linear multistep methods are similar in formulation to Runge-Kutta, however with certain differentiation formulas like BDF they are implicit and so require the use of Newton's method to find the solution with the gradient evaluated at the new time step. This treatment allows them to take fewer steps than an explicit method, though with the caveat that each step takes longer to compute. For stiff differential equations where certain terms result in large variance in the solution, implicit methods end up being much faster despite the additional computation of each step, as explicit solutions require some exorbitant amount of time steps to resolve the equation to an acceptable accuracy. BDF methods can be accurate up to order six however they become less stable as order increases (Süli and Mayers, 2003, pg.349). For a non-linear problem such as this they are only applied with an order of one with some error checking from order two, as beyond this they are no longer A-stable. The

TABLE 2.1: Butcher tableau showing coefficients used for Dormand-Prince method

0							
$\frac{1}{5}$	$\frac{1}{5}$						
$\frac{3}{10}$	$\frac{3}{4}$	$\frac{9}{40}$					
$\frac{4}{5}$	$\frac{44}{45}$	$-\frac{56}{15}$	$\frac{32}{9}$				
$\frac{8}{9}$	$\frac{19372}{6561}$	$-\frac{25360}{2187}$	$\frac{64448}{6561}$	$-\frac{212}{729}$			
1	$\frac{9017}{3168}$	$-\frac{355}{33}$	$\frac{46732}{5247}$	$\frac{49}{176}$	$-\frac{5103}{18656}$		
1	$\frac{35}{384}$	0	$\frac{500}{1113}$	$\frac{125}{192}$	$-\frac{2187}{6784}$	$\frac{11}{84}$	
	$\frac{35}{384}$	0	$\frac{500}{1113}$	$\frac{125}{192}$	$-\frac{2187}{6784}$	$\frac{11}{84}$	0
	$\frac{5179}{57600}$	0	$\frac{7571}{16695}$	$\frac{393}{640}$	$-\frac{92097}{339200}$	$\frac{187}{2100}$	$\frac{1}{40}$

equation for the first order BDF method is given as

$$\mathbf{y}_{n+1} = \mathbf{y}_n + h\mathbf{f}(t_{n+1}, \mathbf{y}_{n+1}) \tag{2.23}$$

To utilise Newton's method this must be rearranged into a form of

$$G(\mathbf{y}_{n+1}) = \mathbf{y}_{n+1} - \mathbf{y}_n - h\mathbf{f}(t_{n+1}, \mathbf{y}_{n+1}) \tag{2.24}$$

which allows Newton's method to find the values of $\mathbf{y}_{n+1}$ that make $G(\mathbf{y}_{n+1}) = 0$ using

$$\mathbf{y}_{n+1}^{k+1} = \mathbf{y}_{n+1}^{k} - J^{-1}(\mathbf{y}_{n+1})G(\mathbf{y}_{n+1}) \tag{2.25}$$

where J is the Jacobian matrix of $G(\mathbf{y}_{n+1})$ given by

$$J(\mathbf{y}_{n+1}) = \begin{bmatrix} \frac{dG_1}{dy_1} & \frac{dG_1}{dy_2} \\ \frac{dG_2}{dy_1} & \frac{dG_1}{dy_2} \end{bmatrix}_{\mathbf{y}_{n+1}} = \begin{bmatrix} 1 - h\frac{df_1}{dy_1} & -h\frac{df_1}{dy_2} \\ -h\frac{df_2}{dy_1} & 1 - h\frac{df_1}{dy_2} \end{bmatrix}_{\mathbf{y}_{n+1}} \tag{2.26}$$

Equation 2.25 is iterated until the difference between two steps is below some predefined tolerance, however for a faster solution an adaptive time step may be used with the amount the step size changes depending on the rate of convergence for the previous step. The terms in the Jacobian can be evaluated analytically and entered into the function but they are calculated faster in this case using explicit finite

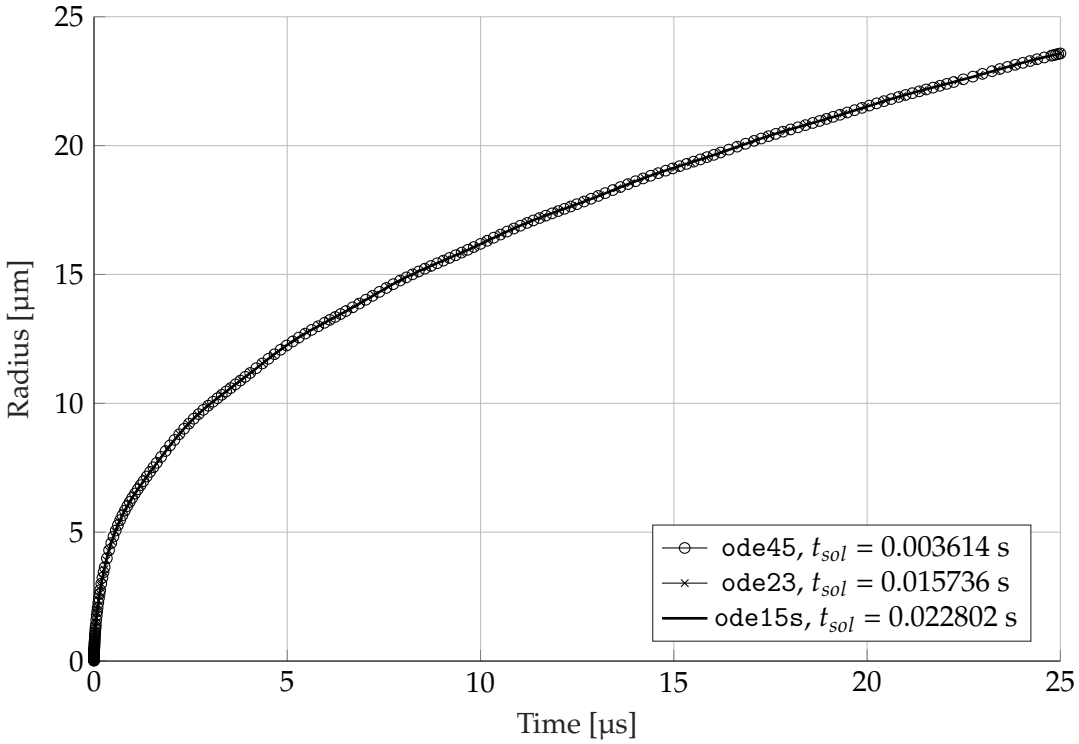

FIGURE 2.3: Comparison of different ODE solvers in MATLAB R2018b using parameters from Event 1 for zero-th order radius molar flow rate.

differences. This method can be implemented using COMSOL or with MATLAB ode15s, though the default scheme for `ode15s` uses the numerical differentiation formula which have different coefficients at higher orders, but for first order accuracy they are identical. Figures 2.3, 2.4, and 2.5 show plots of different solvers computing Equation (2.19) using the various orders of r_B-dependent schemes of n from equation (2.15) for some initial conditions from Event 1 which will be expanded upon in Chapter 3. For comparison, t_sol is the time each solver took to complete the simulation. Of these solvers, `ode45` and `ode15s` have been discussed previously and `ode23` is also an explicit Runge-Kutta method of lower order accuracy.

It can be seen from these figures that the start of the solution requires much smaller time steps than near the end based on the higher concentration of points, and in Figure 2.5 this period makes up a large amount of the final solution. While overall more steps were taken with the explicit methods they were still much faster than `ode15s` by an order of magnitude except for the second order scheme where they are comparable. This is due to the stiff initial growth of the bubble from a small radius that dominates the $\dot{N}_2$ term making the implicit method more efficient. However for all schemes, when the molar flow rate is higher by a couple orders of magnitude the equation becomes very stiff, especially when also increasing the time interval.

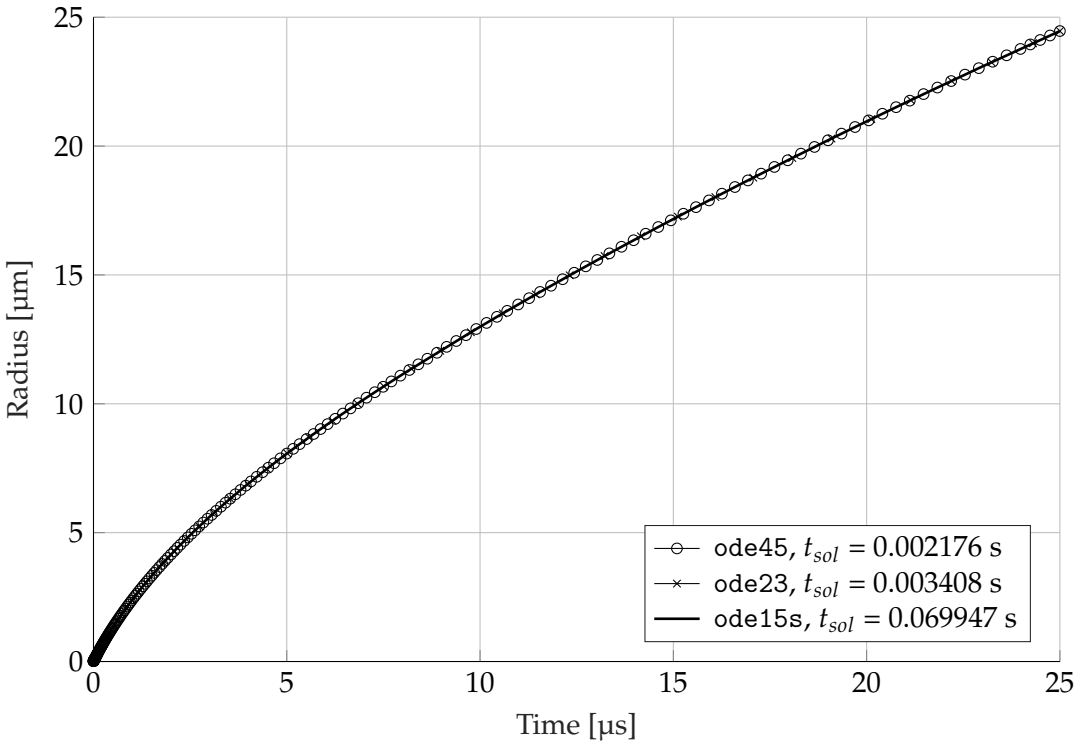

FIGURE 2.4: Comparison of different ODE solvers in MATLAB R2018b using parameters from Event 1 for first order radius molar flow rate.

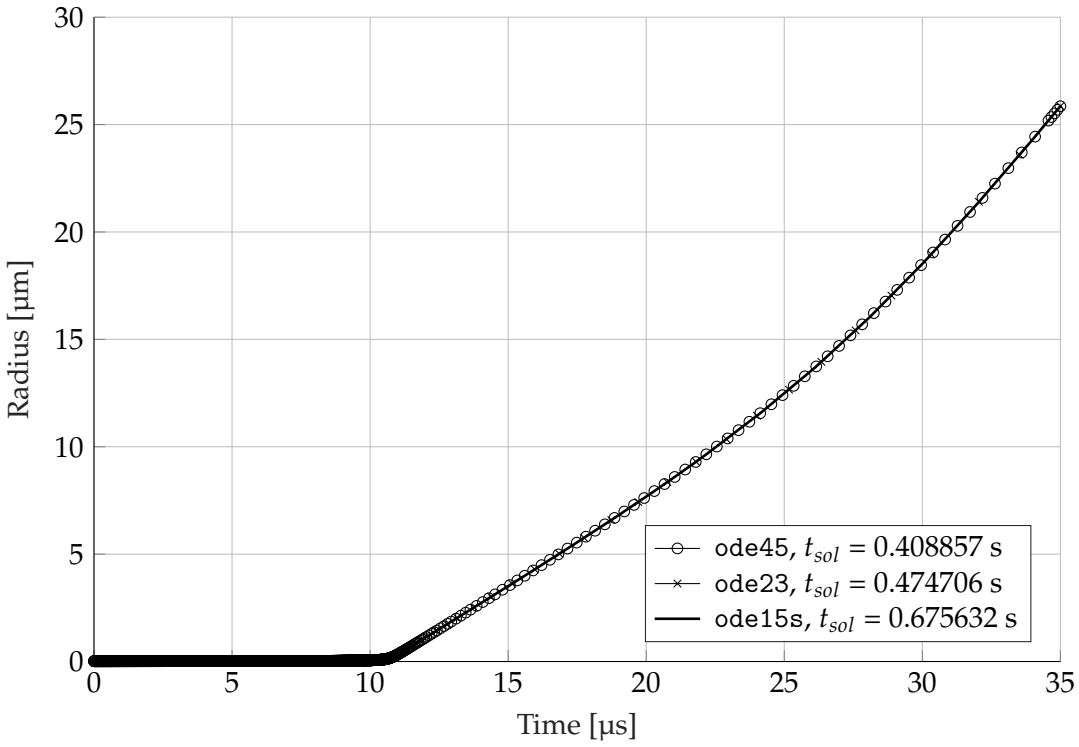

FIGURE 2.5: Comparison of different ODE solvers in MATLAB R2018b using parameters from Event 1 for second order radius molar flow rate.

For example when $\dot{N}_1$ was increased from the usual value for Event 1 of 1.12×10^{-3} mol m^{-1} s^{-1} to 1.12×10^{1} mol m^{-1} s^{-1} with an increased final time of 350 µs, the solutions from explicit methods took prohibitively long at roughly 330 s while `ode15s` solved it in 0.0264 s.

Comparing the final values of bubble radius shows that all solutions converge within a difference of less than 0.01%, giving confidence that each solution method is accurate. As a result, the performance is then gauged by the speed of computation, with `ode45` performing slightly better for the first and second order schemes but much better for zero-th order, `ode45` is chosen for calculating the solutions of the governing ODE in the following sections. This choice is still suitable as the equation becomes stiff for parameters values outside the range of the physical experiments.

2.5 Parameter Sensitivity

In this model there are multiple parameters which are not fully specified like surface tension and temperature. In order to obtain more confidence that the model can capture the physical behaviour of the system the influence of these unclear variables must be calculated. For quantifying the effect of each parameter on the model, the average growth rate of the bubble to the initial droplet radius was used as a standardised value that also allows for comparing the different schemes of molar flow rates. To find this the time array from the numerical solution was interpolated to find the value of time where $r_B = r_{D,0}$ which is then expressed as

$$\bar{q} = \frac{r_{D,0}}{t_{D,0}} \tag{2.27}$$

Figures 2.6, 2.7, and 2.8 show how changing values of surface tension, molar flow rate coefficient, viscosity, and temperature affect the growth rate of the bubble for some range of reasonable parameter values.

All schemes show a similar sensitivity to the parameters. Temperature in the range of values measured by Wainwright et al. (2018) has a slight linear variance in growth rate as it increases. The different values of the molar flow coefficient also contribute to growth rate linearly but with a higher gradient. Viscosity does not have much of a noticeable effect at all with a difference in this range of μ_l = 0.1 mPa s to μ_l = 3 mPa s of less than 0.1% of q for the first order radius scheme. This results in viscosity having a negligible impact on the solution in at least the expected range of values for a liquid metal. Surface tension had the largest effect on growth rate as well as having a decaying exponential profile instead of a linear one like the other parameters, and as expected high surface tension is seen to slow bubble growth.

In Figure 2.6 the first plot shows oscillation of the growth rate at low values of surface tension. This appears to occur at values of $\bar{q}$ greater than 2 m s^{-1} which can also be seen faintly in the plot against molar flow rate. The oscillation is present in

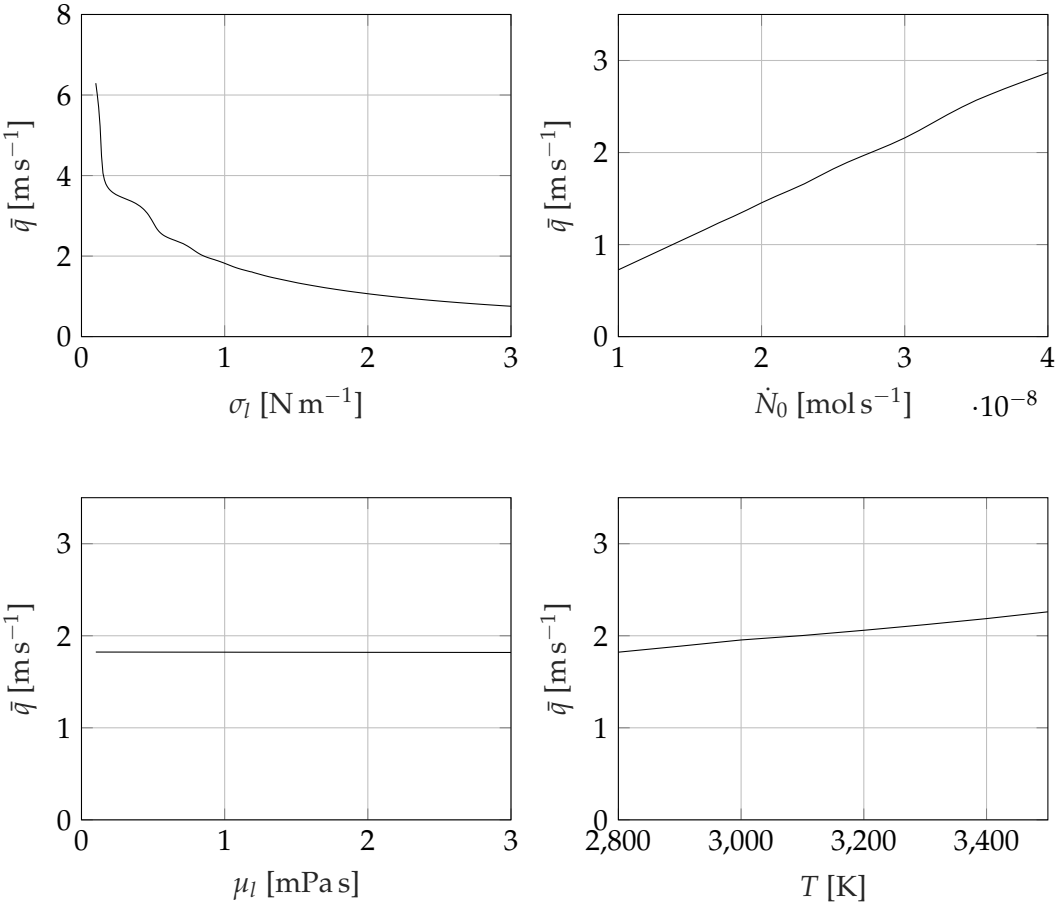

FIGURE 2.6: Parameter sensitivity plots for molar flow rate with zeroth order radius

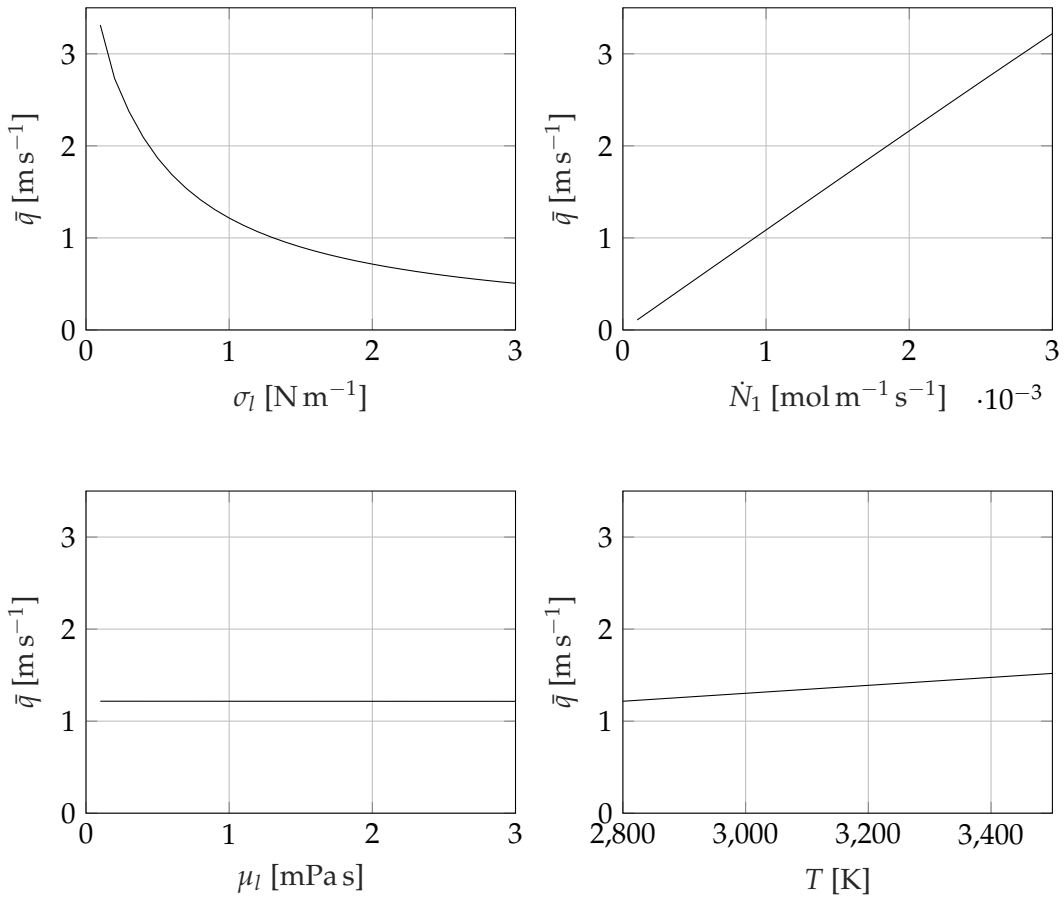

FIGURE 2.7: Parameter sensitivity plots for molar flow rate with first order radius

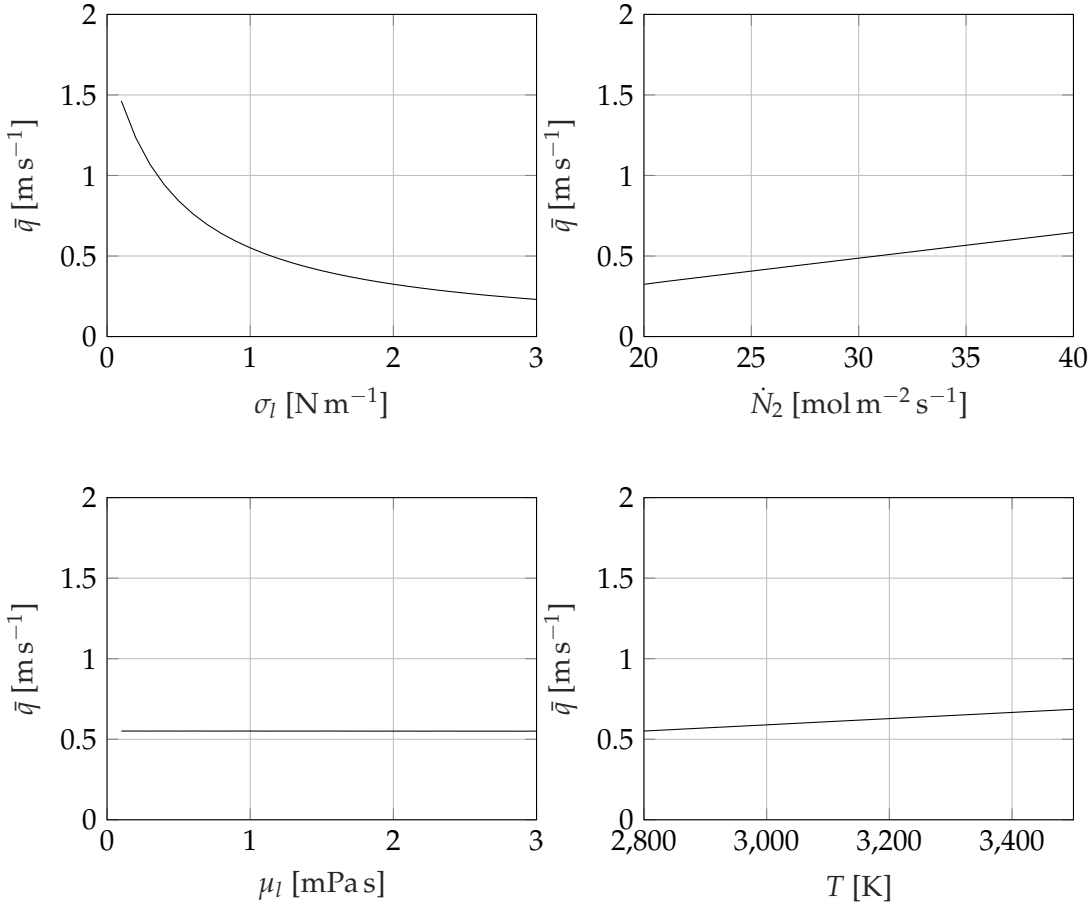

FIGURE 2.8: Parameter sensitivity plots for molar flow rate with second order radius

the solution for radius, with the amplitude increasing with growth rate. It is unclear whether this behaviour is physical or not as there are too few frames in video recordings of the experiments to give enough detail to make a conclusion either way. Some droplets from experiments were recorded with repeated bubbling thought to be caused by puffing but might instead be a result of some other oscillatory behaviour. The oscillations may also be present in lower growth rates but with a much smaller amplitude to the point that it is unnoticeable.

Proper selection of initial conditions for bubble radius, pressure, and growth rate is also important for generating a stable and smooth solution. Starting pressure is a function of the number of molecules of gas in the bubble at the initial radius. To obtain a smooth solution the initial bubble radius needs to be less than 0.1 µm while the initial growth rate does not have as much of an impact and so a value of $2\,\mathrm{m\,s^{-1}}$ was used for all the prior simulations. At such a small starting size for the bubble, the pressure has to be exceedingly large to begin the growth process and this requires specifying an initial pressure of 500 atm. The simulation can be successfully run with a larger intitial radius, for example $r_{B,0} = 1$ µm, which has only minimal oscillations of radius in the early time steps with a starting pressure of 20 atm.

Chapter 3

Bubble Growth Event Analysis

3.1 Introduction

Despite testing the effect of changing the parameters in the model, the simulation must be verified against data observed in experiments. Doing so gives confidence in the veracity of the model and provides a method of estimating the properties of the fluid based on the values that give the best agreement. Additionally, this allows the different schemes for flow rate of nitrogen to be compared which imparts further knowledge on the physical processes that cause microexplosions. The aim of this is to determine which proportionality of radius fits the data best and use that to inform the analysis of diffusion and interfacial adsorption.

3.2 Methods

To obtain the data for bubble radius over time, images of bubble growth events from the experiments done by Wainwright et al. (2019) were located and inspected using Fiji, an image processing package developed by Schindelin et al. (2012) using the ImageJ program. Bubble growth events were defined as a series of frames where the bubble can be seen growing within the droplet from a small initial size for more than two frames. The events terminated with either the microexplosion of the droplet, or the formation of a stable hollow particle. Suitable events had to reasonably match assumptions (1) and (2) for the model, where the droplet contains one bubble that is concentric and spherical.

Once frames with suitable bubble growth events were located, the corresponding droplets were cropped and zoomed in to allow for precise measurements. Figure 3.1 shows a single frame of one recording containing an event. In this image each pixel is $2\,\mu m \times 2\,\mu m$ with a total image width and height of $768\,\mu m$. Figure 3.2 shows the cropped image from Figure 3.1 zoomed in to show a bubble to be measured as part of the event analysis. In this figure, the resolution is $52\,\mu m \times 52\,\mu m$ which allows the boundaries between pixels to be seen clearly. Despite this, it is still unclear exactly where the bubble terminates due to the pixels being relatively large compared to bubbles, as well as low contrast in shades of grey between the liquid metal and

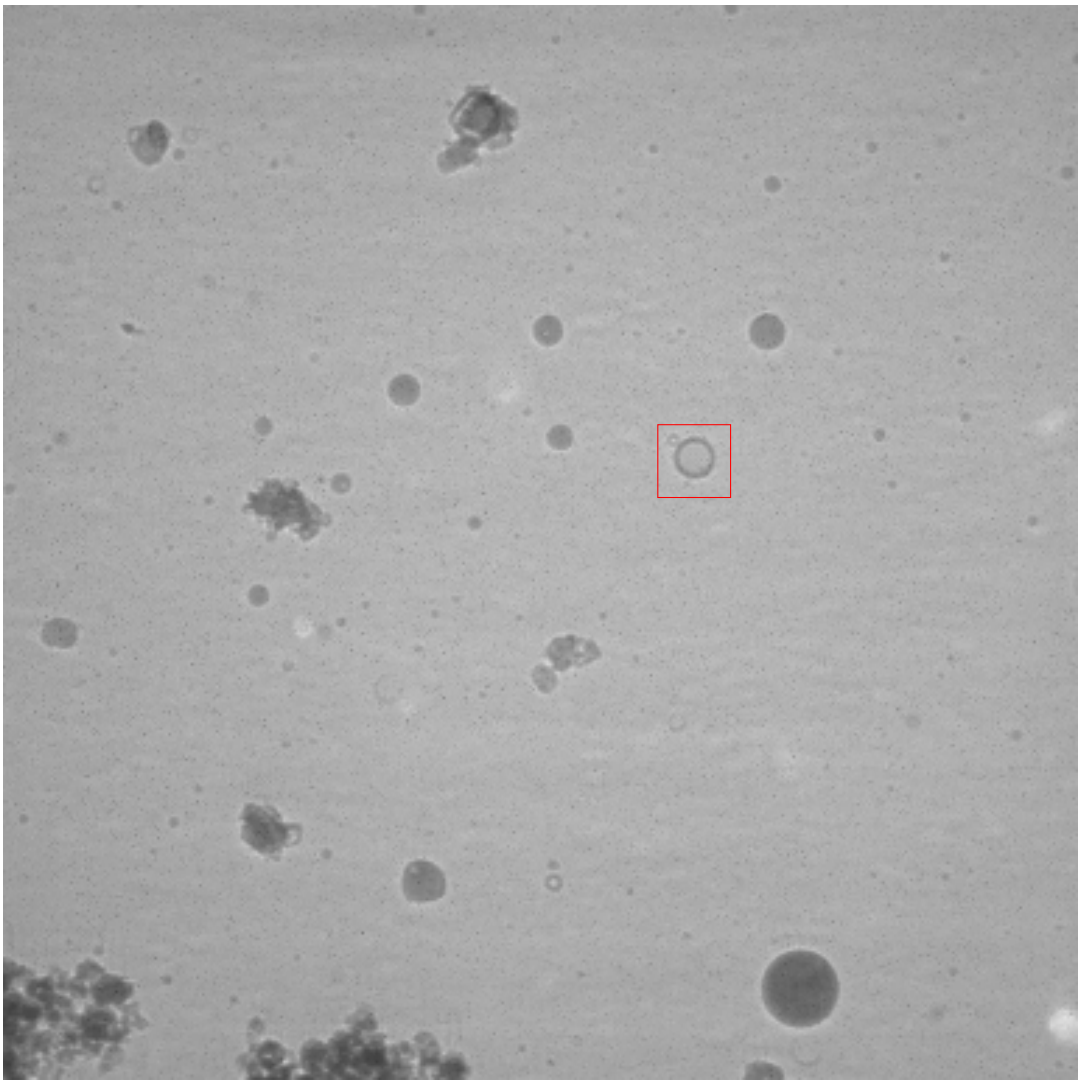

FIGURE 3.1: Still photo of Al:Zr powder combustion from x-ray phase contrast imaging from Wainwright et al. (2019). The particle to be measured is outlined with a square box.

background atmosphere. To account for this uncertainty, measurements were taken by positioning the circle tool in Fiji in a position that best fit the perceived location of the boundary. It was then measured to obtain the area of the bubble which could then be used to calculate the bubble or droplet radii. Measurements were then taken for a circle larger, and then one smaller, by a single pixel in diameter with the difference between them recorded as the experimental uncertainty on the r_B measurement. This procedure is visualised in Figure 3.2 with the drawn circles representing the placements of the circle tool from Fiji.

The average temperature of the combustion reaction is measured around 2700 K – 3500 K as found in Wainwright et al. (2018). With assumption (4) that the temperature is constant throughout the system, a single temperature value is selected for all time steps. This assumes that the temperature is constant over the time period the event occurs in, or that any fluctuation in temperature has a negligible effect on

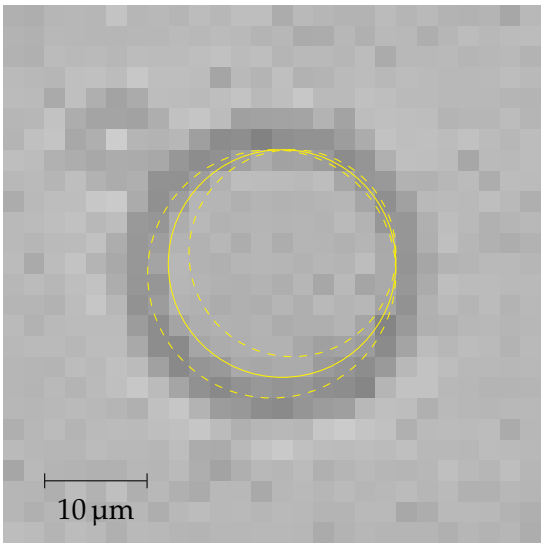

FIGURE 3.2: Unprocessed image from Figure 3.1 cropped to focus on particle for measuring. The full line shows the measured area of the bubble in Fiji using the circle tool. The dashed lines show the increased and reduced measurements for determining the uncertainty bound.

the growth of the bubble. In the model, a value of 2800 K was chosen for the simulation of each event as it is the temperature at which aluminium starts to boil and burn in the vapour phase, and so is the expected lower bound for temperature of the reaction.

Fluid properties for liquid metals of surface tension and viscosity are difficult to evaluate for such high temperatures, which is further complicated by the powders from the experiments being a composite metal consisting of 50:50 aluminium and zirconium. Papers that have measured these parameters experimentally do so at lower temperatures such that the temperature of combustion is far outside the range of interpolation. Despite this, the functions from Paradis et al. (2002) for zirconium and Mills and Su (2006) for aluminium provide an estimate for surface tension of the pure liquid metal, extrapolated to the higher temperature of 2800 K shown in Equations (3.1) and (3.2). The calculation of surface tension for aluminium uses the adopted value for a solution saturated with oxygen which fits with the state of the droplet combustion.

$$\sigma_{Al} = 0.875 - 0.00018\,(T - 933) = 0.54\,\mathrm{N/m} \tag{3.1}$$

$$\sigma_{Zr} = 1.5 - 0.000111\,(T - 2128) = 1.42\,\mathrm{N/m} \tag{3.2}$$

For the composite solution a value for surface tension is estimated to be the average of the values for pure metal, giving 1 N/m which is used in the simulations. Paradis et al. (2002) also provides a function for the viscosity of zirconium

$$\mu_{Zr} = 4.74 - 4.97 \times 10^{-3}(T - 2128) = 1.4\,\mathrm{mPa\,s} \tag{3.3}$$

Dinsdale and Quested (2004) in their review of viscosity data for aluminium cite a value lying between 1 mPa s and 1.4 mPa s to be selected, based on a temperature near the melting point. The viscosity of pure aluminium at the selected temperature would be expected to be lower than this, however with the zirconium increasing the viscosity of the solution, a value of 1 mPa s is selected for solving the model. The density of the solution is estimated to be $\rho_l = 4000\,\mathrm{kg\,m^{-3}}$ as at such high temperatures the density of pure aluminium and zirconium at melting point with a 1:1 atomic ratio would be reduced from the expected value of $5000\,\mathrm{kg\,m^{-3}}$.

Footage of the experiments for the selected bubble events was recorded at 90,000 frames per second, corresponding to 11.11 µs between frames. Within this period it is unknown where the bubble nucleates and starts expanding. In matching the model to the data, a new variable is introduced of Δt_n, which is the time between the start of the solution and the first data point recorded. This variable is chosen alongside $\dot{n}_{r,i}$ for the different schemes to best fit the data within the limits of uncertainty. To accomplish this, the simulation was run multiple times and plotted against the recorded data points. Based on the difference between the results, the parameter values were adjusted in an attempt to reduce the discrepancy at the data points. This process was repeated until the resulting plot of bubble radius for each scheme lay as close as possible to the measured values.

3.3 Results & Discussion

MATLAB R2020a was used to solve the first order coupled ODEs from Equations (2.16) and (2.17) using the function `ode45` for each of the different models for molar flow of nitrogen given by Equation (2.14). The resulting solutions of bubble radius were plotted alongside the measurements from the images for each event in Figures 3.3–3.5. Values of $\dot{N}_i$ and Δt_i for each event were found by trial and error to best fit the data points within the limits of uncertainty of the experimental data. Another more rigorous method involves using Gauss-Newton gradient descent to minimise the residual errors but this failed to fully account for all the error ranges, instead favouring full agreement with two of the data points and neglecting the third. The value of each variable used for the respective events is listed in Table 3.1.

From these plots, it is apparent that the molar flow into the bubble is roughly proportional to r_B of the first order. Event 2 is the closest for the other schemes, but only $\dot{n}_{r,1}$ lies within all the error bars.

After this, the first order scheme was used to perform parametric studies to determine the validity of the model. Small fluctuations of viscosity were found to have a negligible impact on the bubble growth, while temperature, surface tension, and molar flow rate all had significant effects on growth rate. These plots can be seen in Figure 3.6.

TABLE 3.1: List of variables used in simulation of bubble growth events

Variable	Event 1	Event 2	Event 3	Units
$r_{D,0}$	15.0	9.4	10.1	µm
$\dot{N}_0$	2.5×10^{-8}	8×10^{-10}	9.5×10^{-9}	$\mathrm{mol\,s^{-1}}$
$\dot{N}_1$	1.12×10^{-3}	8×10^{-5}	6×10^{-4}	$\mathrm{mol\,m^{-1}\,s^{-1}}$
$\dot{N}_2$	34	4.65	20.5	$\mathrm{mol\,m^{-2}\,s^{-1}}$
Δt_0	0.2	1.6	0.5	µs
Δt_1	1.2	9.5	1	µs
Δt_2	10.4	79	18	µs
$r_{B,0}$	0.02	0.02	0.02	µm
q_0	2	1	3	$\mathrm{m\,s^{-1}}$
t_{max}	25	100	40	µs
$P_{g,0}$	$500P_\infty$	$500P_\infty$	$500P_\infty$	Pa

Given that properties of the metal droplet are somewhat unknown, these plots show that altering these variables only impacts the magnitude of the bubble growth and not the shape of the profile. For any unknowns with regards to temperature or surface tension, there is a value of molar flow rate that could then fit the data. While this means that it becomes impossible to accurately predict the exact rate of nitrogen accumulating in the bubble, it provides confidence that the magnitudes of these properties are reasonably correct and that thefirst order scheme picked for representing molar flow is chosen independent of other parameters in the model.

Applying this method is still imprecise as it is unable to perceive small increments of growth due to the limited spatial resolution of the images, though this affects the validity of data fitting the model with slow bubble growth events much more than with microexplosion events. Despite this there is enough information given by the data within the uncertainty bounds to make inferences about the molar flow into the bubble from the resultant figures, with molar flow appearing to best match the data when linearly proportional to bubble radius.

To obtain more confidence in these findings, it would be beneficial to observe the combustion reaction in experiments with higher temporal and spatial resolutions. A higher frame-rate would allow for a better assessment of the agreement between the model and experiment by increasing the number of data points available. It would also provide more suitable microexplosion events to analyse as there were many instances where microexplosions occurred with only one or two frames of bubble growth, thus a higher frame-rate would be able to capture more data for those events. Meanwhile, increasing the spatial resolution would provide more confidence in the relation by reducing the uncertainty of the bubble measurements with smaller pixels in the recorded image.

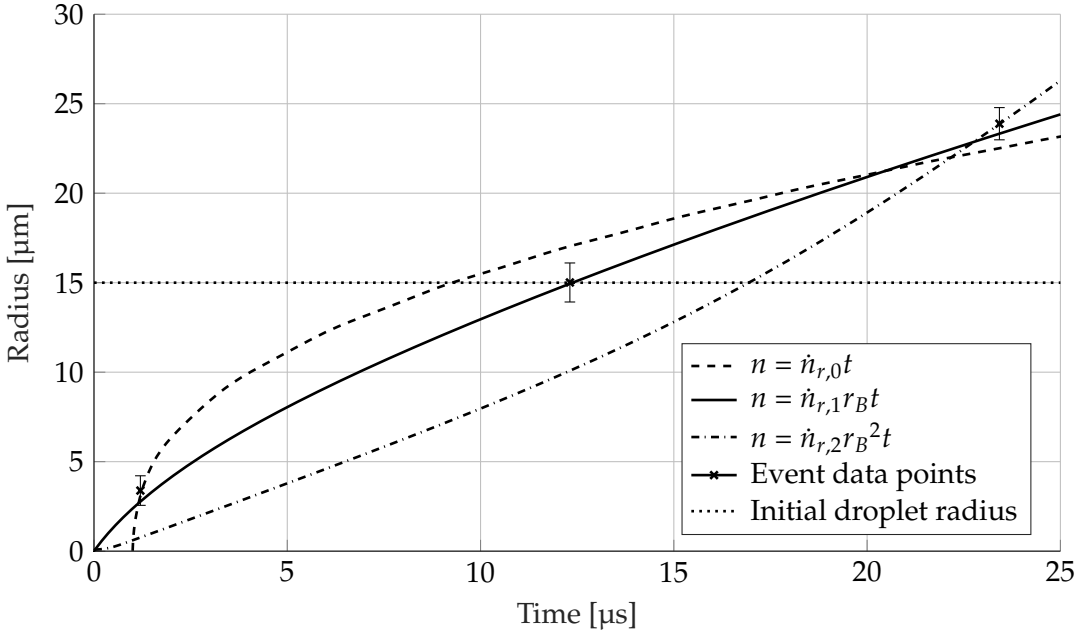

FIGURE 3.3: Bubble growth model for Event 1 solved by `ode45`.

With the technology currently available there are trade-offs between altering the different settings. Increasing frame-rate lowers image resolution while zooming in reduces the chance that an event is in the scope of the camera. To resolve this would require the use of more expensive but higher specification equipment which may not be feasible or even that much of an improvement. Further repetitions of the experiments may help with collecting more data to test the model against which could be all that is necessary. However there are also ways of improving the measured error in the images by using cross correlation methods to achieve sub-pixel accuracy, such as that done by Thielicke (2014). Applying the direct cross correlation algorithm to the recorded events may allow for a more accurate view of the bubble growth process, and then would only require that frame-rate be improved for overall better simulation comparisons.

A better method of fitting the data would be using a Gauss-Newton gradient descent algorithm to minimise the residuals between the model solution and the data points. Applying this method to the current data has limited value compared to manual adjustments due to the inaccuracy of the experimental measurements. Any of the previously discussed methods for recording more precise measurements would make these algorithms more suitable for determining parameter values.

With the apparent first order proportionality of bubble radius, this could be used to compare with the mathematical formulations of the mechanisms of mass transport as a scaling argument, even as the large amount of unknown values preclude the direct calculation of molar flow. Wainwright et al. propose that growth is driven by diffusion of nitrogen from the surface of the droplet through the liquid phase, followed by the adsorption of nitrogen molecules on the bubble-droplet interface.

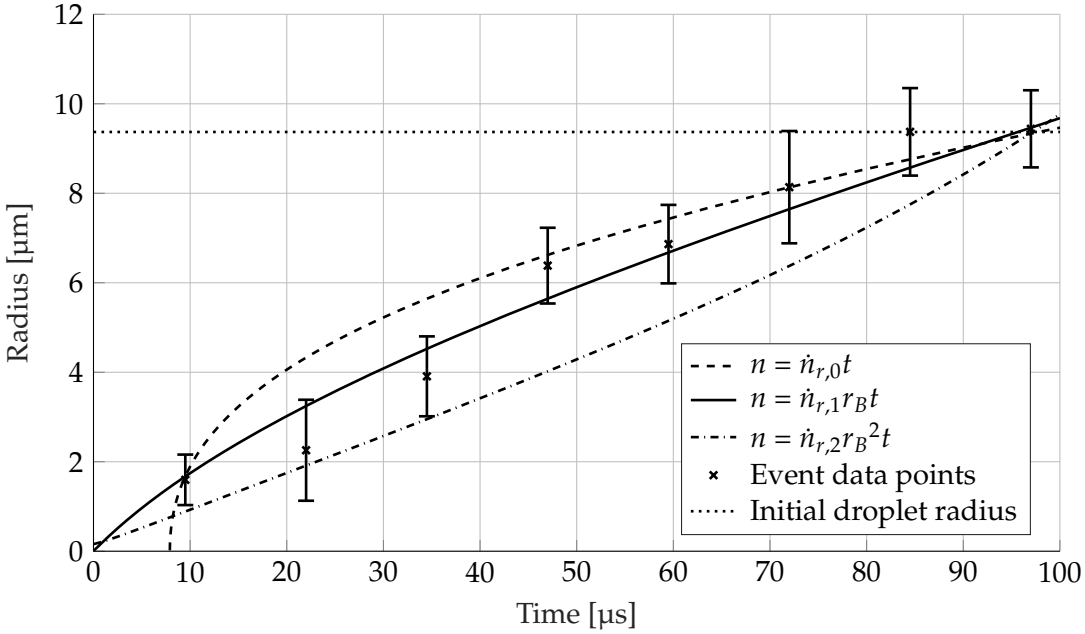

FIGURE 3.4: Bubble growth model for Event 2 solved by `ode45`.

These molecules are then desorbed into the bubble interior. Fick's first law of diffusion states that

$$J = -D\frac{dc_{N_2}}{dr} \tag{3.4}$$

where J is the diffusion flux, D is the diffusivity, and c_{N_2} is the molar concentration of nitrogen in the liquid phase. Taking the overall difference in concentration over the liquid phase and multiplying by the bubble area then gives a scaling argument for the diffusive flow of nitrogen molecules to the bubble interface as

$$\dot{n} \propto -4\pi {r_B}^2 D\frac{c_{N_2,D} - c_{N_2,B}}{r_D - r_B} \tag{3.5}$$

This can be seen to have a first order dependence of bubble radius, with the denominator being some other function of bubble radius that cancels out the squared term from the area. In order to test this, the values of diffusivity and concentrations would need to be found which would be difficult for the same reasons as finding surface tension and viscosity of the liquid. Without any information known about these variables it is impossible to infer anything about this mechanism as the values of concentration and diffusivity may also depend on radius, which could alter the overall proportionality of molar transfer.

For interface desorption, Chen (2020) solves Fick's second law of diffusion as the rate of collisions of the solute integrated over surface for a specified time. The solution takes the form of

$$\dot{n} = c_{N_2,l} A_B \sqrt{\frac{D}{\pi t}} \tag{3.6}$$

where $c_{N_2,l}$ is the bulk concentration of nitrogen in the liquid phase, A_b is the surface

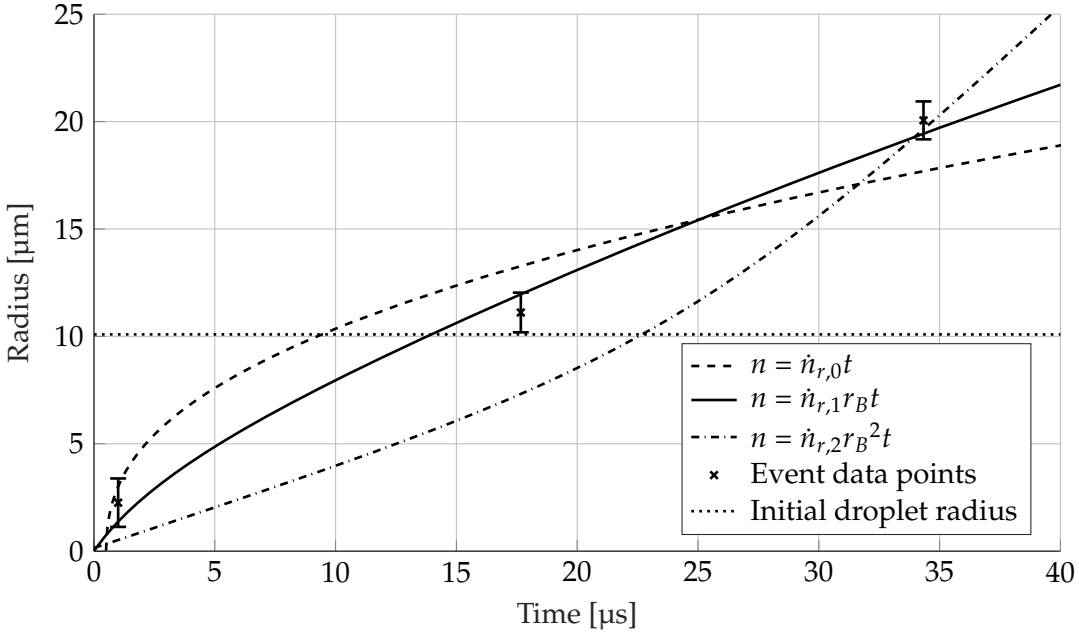

FIGURE 3.5: Bubble growth model for Event 3 solved by `ode45`.

area of the bubble interface, and t is the time that has elapsed since the start of adsorption. While it appears to have a second order dependence of radius from area, it is also inversely proportional to time which may allow for a linearly proportional molar flow as it counteracts the influence of the squared radius term.

3.4 Conclusions

This chapter investigates the bubble growth within combusting metal droplets and compares the data from experimental recordings with a numerical model. The mathematical model is derived from the Navier-Stokes momentum equation reduced to an ordinary differential equation for the bubble radius based on equilibrium of forces at the bubble-droplet and droplet-air interfaces. Still frames of bubble growth events from experiments were found with the size of the bubble at each frame measured manually. Different functions for calculating the amount of moles of nitrogen flowing into the bubble were created for comparison with the data. From the figures produced by the model solutions it can be seen that the molar flow rate of nitrogen fits the data best when it is linearly proportional to the bubble radius. Repeating the experiment with a higher resolution recording set up would allow us to gain more confidence in these findings. Alternatively, applying cross correlation methods could improve the precision of measurements of the current experimental images. Improving the accuracy would allow for gradient descent algorithms to find precise values of parameters that minimise residuals between the model solution and data points. Based on the scaling argument, diffusion limited transport is more likely to fit the observed first order proportionality, however the numerous uncertainties in the model cannot entirely preclude the other processes from consideration.

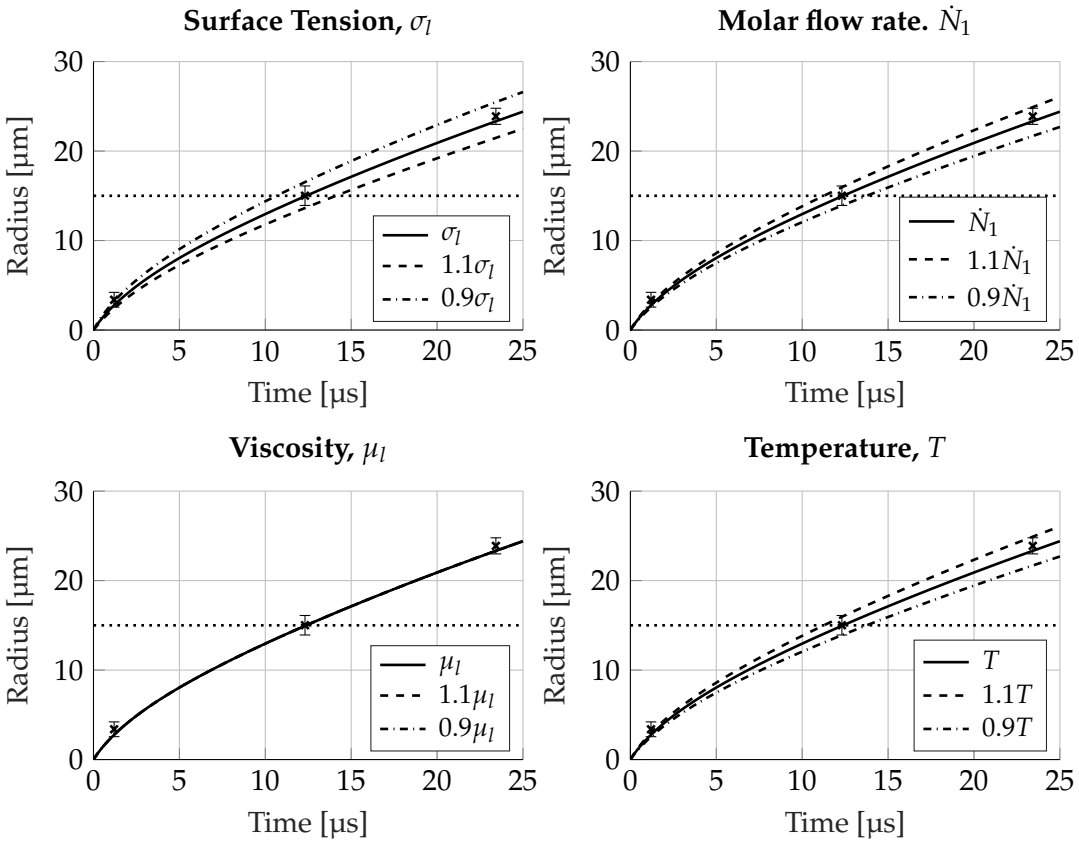

FIGURE 3.6: Bubble growth model for Event 1 solved by `ode45` for changes of value 10% higher and lower for different parameters.

Chapter 4

Multidimensional Simulation

4.1 Introduction

Following the results obtained from the ordinary differential equation simulation, the system was modelled in 2D-axisymmetric to compare with and attempt to validate the assumptions that allowed it to be reduced to Equation (2.9). Of particular interest are the effect that off centre bubble nucleation has on growth and calculating the velocity profile throughout the liquid phase. Other assumptions regarding the bubble and droplet being spherical and the mass continuity substitution for the velocity of the interface can also be verified.

The model extended to multiple dimensions was built using COMSOL Multiphysics version 5.5. COMSOL is a finite element solver and multiphysics simulator that can solve systems of coupled partial differential equations. This makes it suitable for applying to this problem as the governing equation is the full Navier-Stokes.

The finite element method solves the governing equation by reducing it to a weak form using integration after multiplying the terms by some test function. In vector form the incompressible Navier-Stokes momentum equation is

$$\rho\frac{\partial \boldsymbol{u}}{\partial t} + \rho\left(\boldsymbol{u}\cdot\nabla\boldsymbol{u}\right) = -\nabla p + \mu\Delta\boldsymbol{u} + \boldsymbol{f} \tag{4.1}$$

$$\nabla\cdot\boldsymbol{u} = 0 \tag{4.2}$$

where

$$\boldsymbol{u}(x,y) = \begin{bmatrix} u & v \end{bmatrix}$$

in which u is the velocity component of the fluid in the x direction and v is the velocity component for the y direction. Then with all terms in Equation 4.1 multiplied by the test function $\boldsymbol{v}$, which is suitably defined in some space V, integrate over the domain Ω to get

$$\int_\Omega \rho\frac{\partial \boldsymbol{u}}{\partial t}\boldsymbol{v}dV + \int_\Omega \rho\left(\boldsymbol{u}\cdot\nabla\boldsymbol{u}\right)\boldsymbol{v}dV = -\int_\Omega \nabla p\boldsymbol{v}dV + \int_\Omega \mu\nabla^2\boldsymbol{u}\boldsymbol{v}dV + \int_\Omega \boldsymbol{f}\boldsymbol{v}dV \tag{4.3}$$

then using Green's first identity to reduce the order of the diffusive term yields

$$\int_\Omega \mu \nabla^2 \boldsymbol{u} \boldsymbol{v} dV = \int_{\partial\Omega} \mu \nabla \boldsymbol{u} \cdot \boldsymbol{n} \boldsymbol{v} dS - \int_\Omega \mu \nabla \boldsymbol{u} \cdot \nabla \boldsymbol{v} dV \tag{4.4}$$

which when substituted into Equation 4.3 gives

$$\begin{aligned}\int_\Omega \rho \frac{\partial \boldsymbol{u}}{\partial t} \boldsymbol{v} dV + \int_\Omega \rho \left(\boldsymbol{u} \cdot \nabla \boldsymbol{u}\right) \boldsymbol{v} dV = &- \int_\Omega \nabla p \boldsymbol{v} dV + \int_{\partial\Omega} \mu \nabla \boldsymbol{u} \cdot \boldsymbol{n} \boldsymbol{v} dS \\ &- \int_\Omega \mu \nabla \boldsymbol{u} \cdot \nabla \boldsymbol{v} dV + \int_\Omega \boldsymbol{f} \boldsymbol{v} dV \qquad \forall \boldsymbol{v} \in V \end{aligned} \tag{4.5}$$

This substitution is used to reduce the order of continuity required for the solution $\boldsymbol{u}(x, y)$. Applying this same process with a test function q in a space Q to the continuity equations results in its weak form of

$$\int_\Omega q \nabla \cdot \boldsymbol{u} dV = 0 \qquad \forall q \in Q \tag{4.6}$$

The domain is then divided into a series of 2D elements with nodes at each corner point. This allows the solution to be expressed by the sum of discrete values of $\boldsymbol{u}$ at each node point multiplied by the corresponding shape function over the element which is

$$\boldsymbol{u}(x, y) = \sum_{i=1}^{n} N_i \boldsymbol{u}_i \tag{4.7}$$

where $\boldsymbol{u}_i$ is the value of the velocity vector at node i, N_i is the corresponding interpolation function at that node and n is the total number of nodes in the domain. This form can be used to express the values of p, and $\boldsymbol{f}$ as well. The Galerkin method assumes that the test function becomes the interpolation function such that $\boldsymbol{v} = N_j$ for $j = 1, \ldots, n$. Substituting these expressions into Equation 4.5 yields

$$\begin{aligned}\int_\Omega \rho \frac{\partial}{\partial t} \left(\sum_{i=1}^{n} N_i \boldsymbol{u}_i \right) N_j dV + \int_\Omega \rho \left(\left(\sum_{i=1}^{n} N_i \boldsymbol{u}_i \right) \cdot \nabla \left(\sum_{i=1}^{n} N_i \boldsymbol{u}_i \right) \right) N_j dV \\ = - \int_\Omega \nabla \left(\sum_{i=1}^{n} N_i p_i \right) N_j dV + \int_{\partial\Omega} \mu \nabla \left(\sum_{i=1}^{n} N_i \boldsymbol{u}_i \right) \cdot \boldsymbol{n} N_j dS \\ - \int_\Omega \mu \nabla \left(\sum_{i=1}^{n} N_i \boldsymbol{u}_i \right) \cdot \nabla N_j dV + \int_\Omega \left(\sum_{i=1}^{n} N_i f_i \right) N_j dV \end{aligned} \tag{4.8}$$

Then the summation schemes are transformed into matrix products which are rewritten as

$$\sum_{i=1}^{n} N_i \boldsymbol{u}_i = M \vec{\boldsymbol{u}} = \begin{bmatrix} N_1 & \cdots & N_n \end{bmatrix} \begin{bmatrix} u_1 & v_1 \\ \vdots & \vdots \\ u_n & v_n \end{bmatrix} \tag{4.9}$$

$$\nabla\left(\sum_{i=1}^{n} N_i \boldsymbol{u}_i\right) = \nabla M\vec{\boldsymbol{u}} = \begin{bmatrix} \nabla N_1 & \cdots & \nabla N_n \end{bmatrix} \begin{bmatrix} u_1 & v_1 \\ \vdots & \vdots \\ u_n & v_n \end{bmatrix} \tag{4.10}$$

which are then put back into Equation 4.8 and rearranged to get the matrix form of

$$\begin{aligned} \rho \int_\Omega \left(M\frac{\partial \vec{\boldsymbol{u}}}{\partial t}\right) N_j dV + \int_\Omega \rho\left((M\vec{\boldsymbol{u}})\cdot(\nabla M\vec{\boldsymbol{u}})\right) M dV = -\int_\Omega (\nabla M\vec{p})\, M dV \\ + \mu \int_{\partial\Omega} (\nabla M\vec{\boldsymbol{u}})\cdot \boldsymbol{n} M dS - \int_\Omega \mu\,(\nabla M\vec{\boldsymbol{u}})\cdot\nabla M dV + \int_\Omega \left(M\vec{f}\right) M dV \end{aligned} \tag{4.11}$$

This can then be rearranged into a system of equations represented by

$$\boldsymbol{K}\begin{bmatrix} \vec{\boldsymbol{u}} \\ \vec{p} \end{bmatrix} = \boldsymbol{b} \tag{4.12}$$

so that the system can be solved using well known matrix solvers to find the values of $\vec{\boldsymbol{u}}$ and $\vec{p}$. The Navier-Stokes equations are non-linear so the $\boldsymbol{b}$ vector also contains terms involving $\vec{\boldsymbol{u}}$ and $\vec{p}$ which requires additional steps to calculating the solution. The time stepping of the problem is solved in COMSOL using the BDF method which was discussed in Chapter 2.

4.2 Method

Modelling the droplet system was performed using a 2D-axisymmetric model with Laminar Flow and Moving Mesh under a Time Dependent study. 2D-axisymmetric is used to exploit the axial symmetry of the bubble and droplet, reducing the computational cost a significant amount by removing a further dimension. In doing this simplification, the fluxes of dependent variables normal to the 2D plane in the θ direction are treated as equal (or zero) to preserve the symmetry. This symmetry condition does require that offset bubble nucleation only occurs along the symmetrical axis, as otherwise the 3D geometry would no longer be spherical. The moving mesh is required as the bubbles expansion over time will change the sizes of the domain.

The geometry of the system was then generated using two circles based at the centre with radii of $r_{B,0}$ for the bubble and $r_{D,0}$ for the droplet and joined together using a union. Parts of the geometry on the left side of the axis where $r < 0$ were subtracted using a difference to leave two concentric semicircles shown in Figure 4.1, that when rotated in the θ direction around the axis of symmetry at $r = 0$ form spherical objects as desired.

The bubble domain was specified as being nitrogen and the liquid domain was represented by a user-defined fluid with viscosity μ_l and density ρ_l. Boundary conditions were specified in the Laminar Flow branch and required the Microfluidics

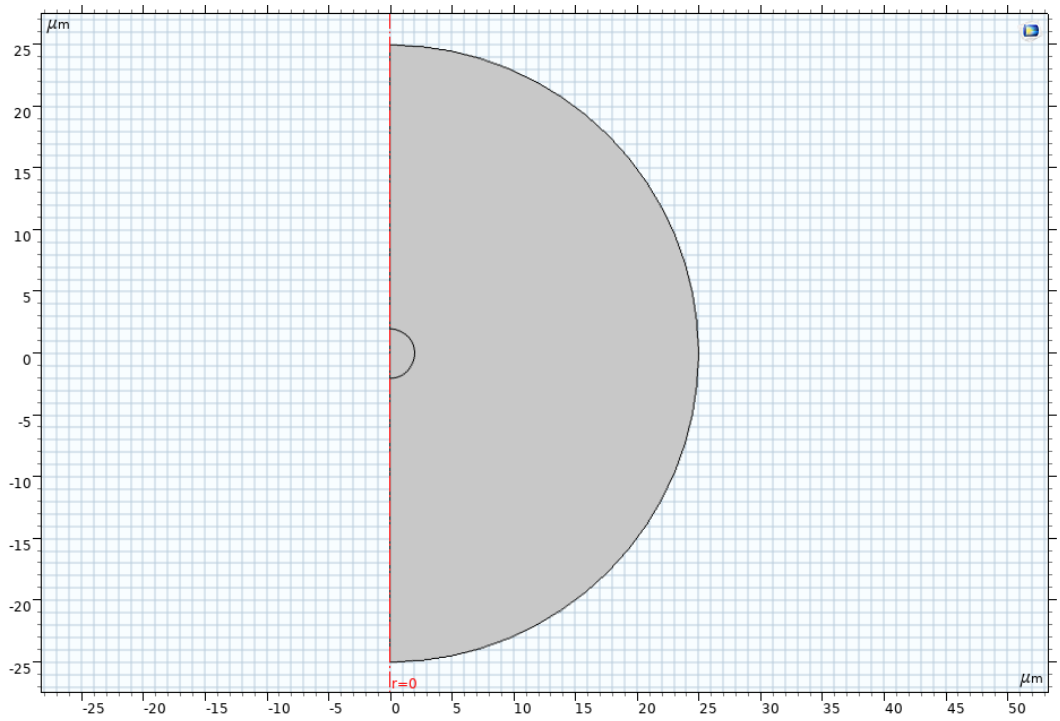

FIGURE 4.1: Image of geometry for representing the bubble-droplet system

package to add an external fluid interface at the outer boundary, and a fluid-fluid interface at the internal boundary. In addition, the flat side of the semicircle on the axis at $r = 0$ had a specified axial symmetry condition. These boundary conditions model the influence from surface energy caused by the interfaces between fluids, where the fluid-fluid boundary is between nitrogen and the liquid metal while the external boundary is between the liquid metal and air. For both interfaces the surface tension was input as σ_l and for the internal boundary there is a mass flux to model the flow of nitrogen into the bubble.

The mass flux differs from solving the ODE in MATLAB, in which the amount of nitrogen at a given time is calculated using a fixed molar rate. In addition, the COMSOL domain is a infinitesimal wedge of the entire 3D bubble, which in the θ direction continues over 2π radians. Comparing the ODE and 2D solutions then requires the expression for $\dot{n}_1$ to be rearranged for flux and multiplied by the number of radians such that

$$J_m = 2\pi \frac{\dot{N}_1 r_B M_{N_2}}{A_B} = \frac{\dot{N}_1 M_{N_2}}{2r_B} \tag{4.13}$$

where M_{N_2} is the molar mass of nitrogen gas and J_m is the mass flux. Due to the system of equations being highly non-linear, the mass flux as the primary forcing term was multiplied by a step function that smoothly ramps up from zero to one over a tenth of a microsecond. This was implemented in order to aid the transition from initial conditions and improve convergence.

With the boundary conditions set, the mesh could then be generated. The bubble

TABLE 4.1: List of variables used in ODE simulation for COMSOL comparison

Quantity	Variable	Value	Units
Initial droplet radius	$r_{D,0}$	25.0	µm
Molar flow rate per metre	$\dot{N}_1$	3×10^{-4}	$\mathrm{mol\,m^{-1}\,s^{-1}}$
Initial bubble radius	$r_{B,0}$	0.05	µm
Initial bubble growth rate	q_0	0.5	$\mathrm{m\,s^{-1}}$
Maximum time elapsed	t_{max}	100	µs
Initial bubble pressure	$P_{g,0}$	$400P_{\mathrm{inf}}$	Pa
Surface tension	σ_l	1.0	$\mathrm{N\,m^{-1}}$
Viscosity	μ_l	1.0×10^{-3}	Pa s
Temperature	T	2800	K

domain was built using a free-triangular mesh and the liquid domain was built with a mapped quadrilateral mesh. The element size was set to the "Fine" preset and calibrated for fluid dynamics. The free triangular mesh allowed the bubble domain to expand uniformly while the mapped mesh meant that compression of the domain in the liquid did not skew the element quality too much. Two refinement nodes were added to the mesh, with two regular refinements applied to the bubble domain and a single edge refinement applied to the symmetrical and fluid-fluid boundaries. These settings resulted in the mesh shown in Figure 4.2.

In setting initial conditions, a simulation was run using the ODE to estimate the starting values. Fluid properties used in this simulation are consistent with values from the event analysis with all parameters required listed in Table 4.1.

Using these parameters for solving the ordinary model with MATLAB `ode15s` resulted in the plots for radius, growth rate, and pressure shown in Figure 4.3. The 2D model in COMSOL is very sensitive to the starting values with slightly disparate initialisation values causing the solution to fail. It also has trouble with small initial bubble sizes and so the COMSOL models use an initial bubble radius of $r_{B,0} = 2\,\mu\mathrm{m}$. The value of pressure at this radius from the ODE was found to be 11.832 bar which is then input to the initial value of pressure in the bubble in the COMSOL model. The velocity field is left with an initial value of zero as the bulk of the fluid in both the liquid and gas phases starts out stationary.

In addition to the concentric study, a parametric sweep was set up to evaluate the growth of bubbles nucleated at varying distances from the droplet centre. This offset centre point of the bubble was expressed as a ratio of the initial droplet radius as

$$\zeta = \frac{l_B}{r_{D,0}} \tag{4.14}$$

for a possible range from zero to one as l_B goes from zero to $r_{D,0}$, however the bubble

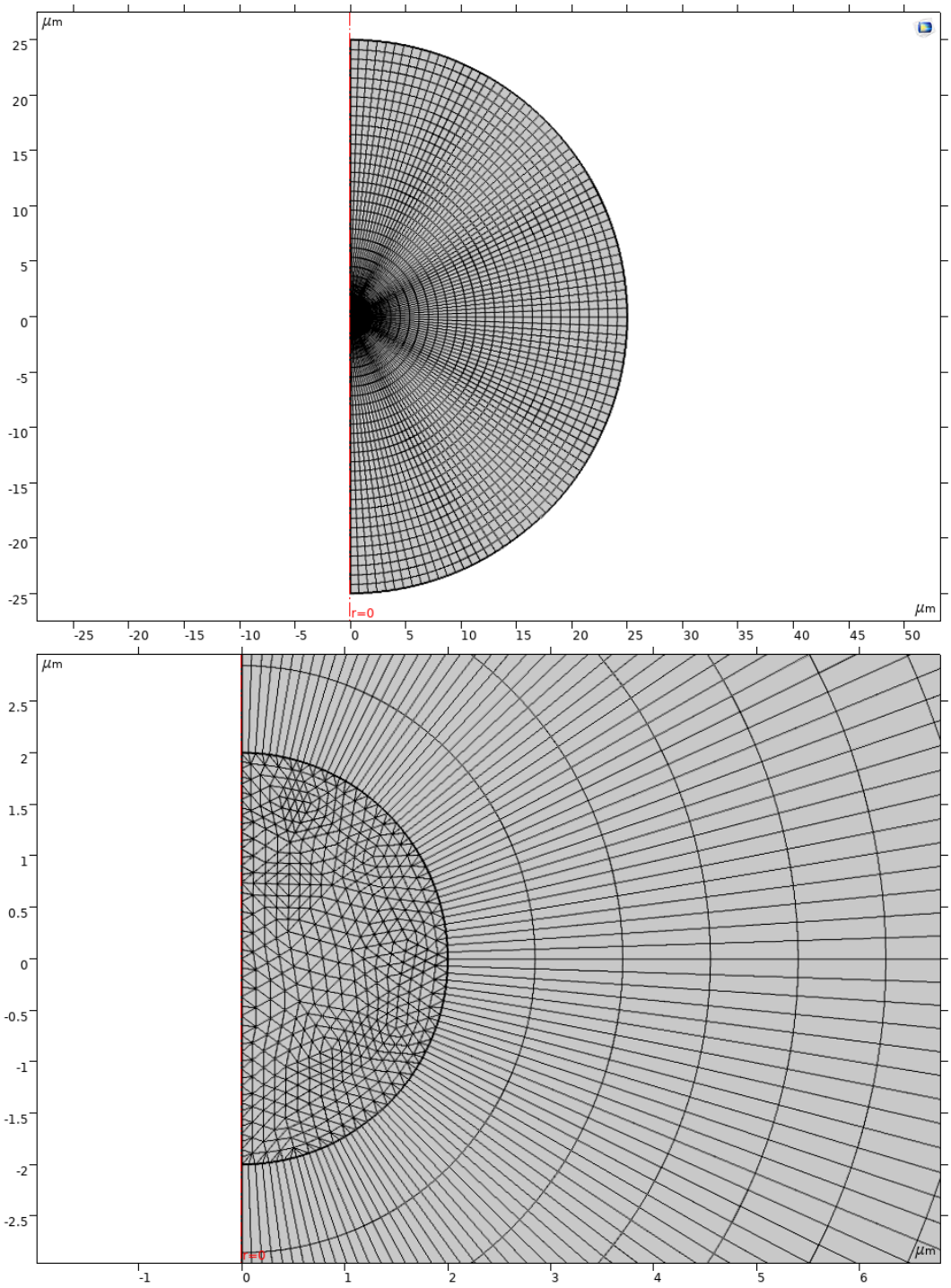

FIGURE 4.2: Images of the mesh used for calculating the system of equations. The top image shows the mesh over the full geometry while the bottom image zooms in to the bubble domain to show the boundaries in detail.

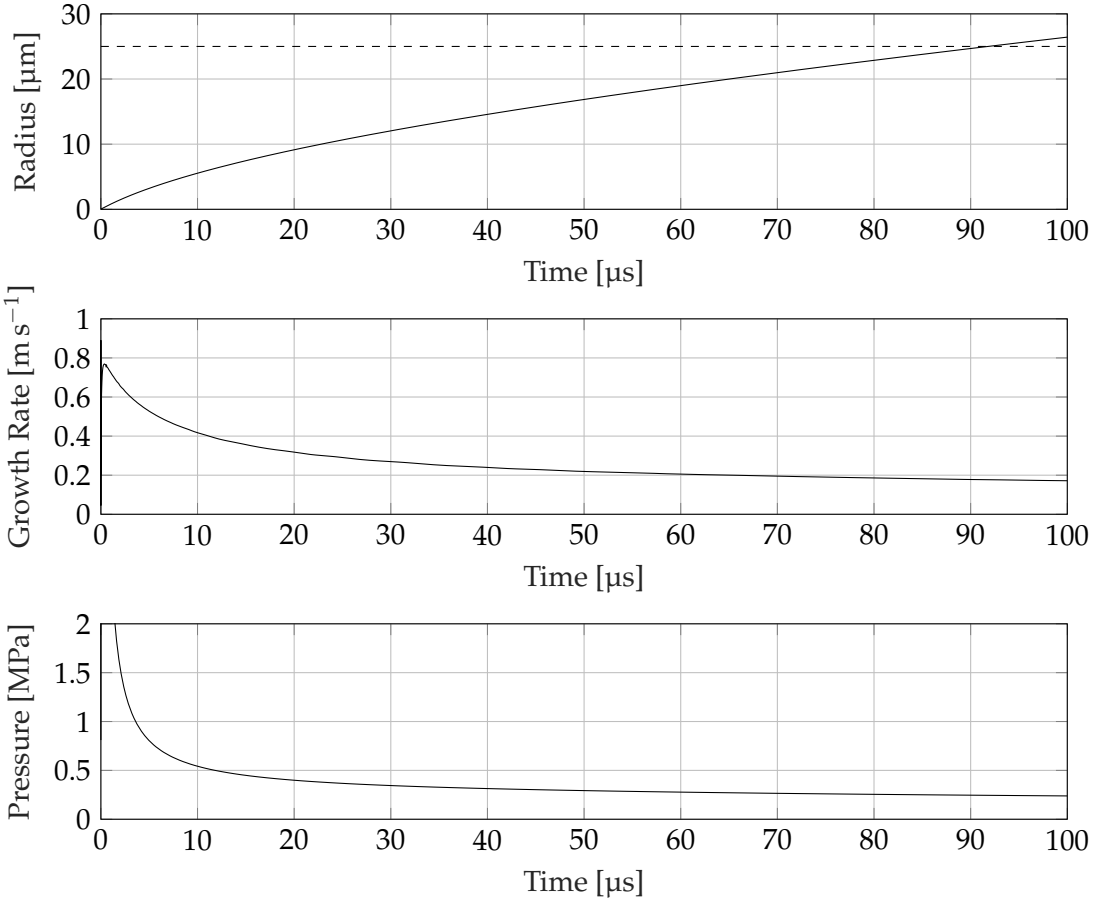

FIGURE 4.3: Plots of bubble radius, growth rate, and pressure from ODE simulation to obtain consistent initial values for COMSOL.

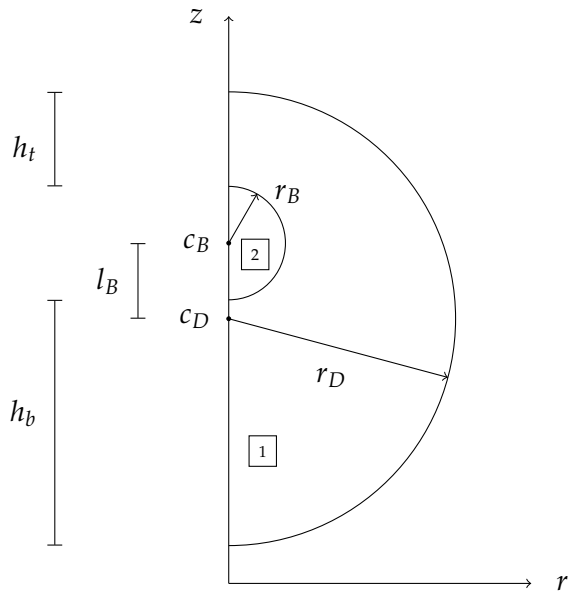

FIGURE 4.4: Diagram showing key dimensions for tracking evolution of the system as the bubble expands.

centre will never be exactly on the outer edge of the droplet and those that grow close to the edge will puff instead of exploding. As such, the initial position of the bubble centre which was concentric with the droplet was shifted up the z axis by $l_B = \zeta r_{D,0}$ for a range of $\zeta = 0, 0.05, 0.10, \ldots, 0.30$. Larger values of ζ resulted in the solution failing to converge and so the study was only explored on the range of $0 < \zeta < 0.3$.

Multiple probes were created to measure the different dimensions of the system as it evolved. These used the `maxop` functions to evaluate the highest and lowest values of position coordinates in the selected domains. By doing so, the dimensions of interest could be evaluated using averages between the r and z directions to account for any cases where the domain may become spatially non-spherical.

In the diagram shown in Figure 4.4, Domain 1 represents the liquid metal phase of the droplet while Domain 2 is the gaseous bubble. Assuming that they stay approximately circular their respective radii can be evaluated using the $\texttt{maxop}(f, x)$ function in COMSOL, which finds location of the maximum value of some function, f, in the specified dimension, x. This was used to find the highest and lowest points of z in the domain and also the maximum r point. The radius for the droplet or bubble can then be calculated using the formula

$$r = \frac{\texttt{maxop}(r, r) + \dfrac{\texttt{maxop}(z, z) - \texttt{maxop}(-z, z)}{2}}{2} \tag{4.15}$$

which averages the values of maximum r and z dimensions with the minimum z to approximate the radius assuming the domains remain circular. For the droplet radius, r_D is found using `maxop1` applied to Domain 1 and similarly the bubble radius r_B is found using `maxop2` applied to Domain 2. As mentioned before, this approach

assumes that the domain remains approximately circular throughout the simulation as it only uses three points in the formula. Comparing the measurements reveals that the maximum relative error between the z and r operations is 0.0209% for the droplet radius and 0.0313% for the bubble radius, with the averages slightly under that at 0.0145% and 0.0256% respectively. These low differences between the measurements show that the assumption is valid and so this method was used to record the values of radii from the COMSOL solution. Another method that was trialled involved using the curvature evaluation but that was found to be inconsistent with the moving mesh module.

Other dimensions shown in Figure 4.4 are also calculated using the `maxop` functionality. The centre points of the domains c_D and c_B are found using

$$c = \frac{\texttt{maxop}(z,z) + \texttt{maxop}(-z,z)}{2} \tag{4.16}$$

on their respective domains. The thickness of the liquid domain at the top and the bottom of the system given by h_t and h_b are evaluated with the formulae

$$h_t = \texttt{maxop1}(z,z) - \texttt{maxop2}(z,z) \tag{4.17}$$

$$h_b = \texttt{maxop1}(-z,z) - \texttt{maxop2}(-z,z) \tag{4.18}$$

noting that `maxop1` refers to Domain 1 and `maxop2` refers to Domain 2. The ratio between the two values is defined as

$$\gamma = \frac{h_b}{h_t} \tag{4.19}$$

and indicates how evenly distributed the liquid phase is distributed around the droplet.

4.3 Results & Discussion

4.3.1 ODE Comparisons

In expanding the simulation to 2D, the growth of the bubble is best visualised using a surface plot, such as those shown in Figure 4.5 for a concentric bubble. This figure is generated by plotting velocity profiles at discrete times of the solution to show how the velocity changes over time. At the beginning of growth there is a sharp velocity gradient and acceleration around the bubble when growth is fastest. As the bubble expands, the overall magnitude reduces, but the outer region of the liquid phase also starts to expand with the gradient decreasing over time. Within the bubble, the expansion seems not to cause a resultant velocity profile, possibly due to the molecules of nitrogen expanding uniformly as more mass enters the domain at the boundary, though it may also be due to the effect being too small to notice when

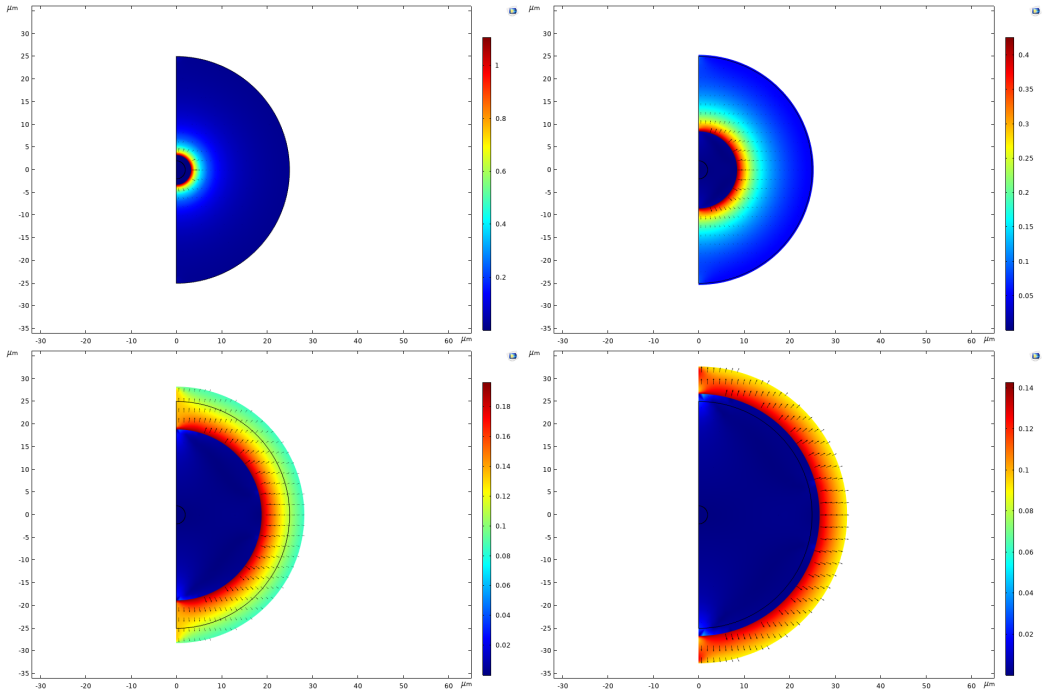

FIGURE 4.5: Surface plots of velocity magnitude for concentric bubble growth at times of 1 µs, 10 µs, 50 µs, and 100 µs respectively.

scaled with the liquid domain. In the profile at 50 µs and 100 µs some numerical artifacts appear around the axis of symmetry near the poles. While the presence of these artifacts may impact the solution adversely, further refining the mesh to eliminate them only results in the solution failing to converge so they cannot be removed entirely.

In the initial model it was assumed that conservation of mass caused the droplet radius to be implicitly linked to its initial size and the bubble radius. Figure 4.6 shows plots of this relationship calculated with the expression applied to the probed value of bubble radius and with the probed value of droplet radius. Inspecting the plot reveals that the two methods of obtaining the droplet radius are markedly similar, giving confidence to the prior assumption when applied to the ODE.

The probed bubble radius was plotted against the ODE solutions from Table 4.1 resulting in Figure 4.7. As the COMSOL simulation required increasing the size of the initial bubble from the ODE values, the ODE was evaluated again from the same starting conditions as the COMSOL model. It can be seen in this figure that the profile of bubble radius between COMSOL and the ODE is similar despite a shift up in value of the COMSOL solution that decreases as time continues, eventually yielding the same final radius. The behaviour of the ODE at different initial conditions is interesting as it does not follow the COMSOL solution, instead converging to the better initialised ODE solution at around 30 µs.

Comparing these different methods also requires evaluating the pressure profiles as the primary forcing term on bubble growth. These plots are shown in Figure 4.8. A

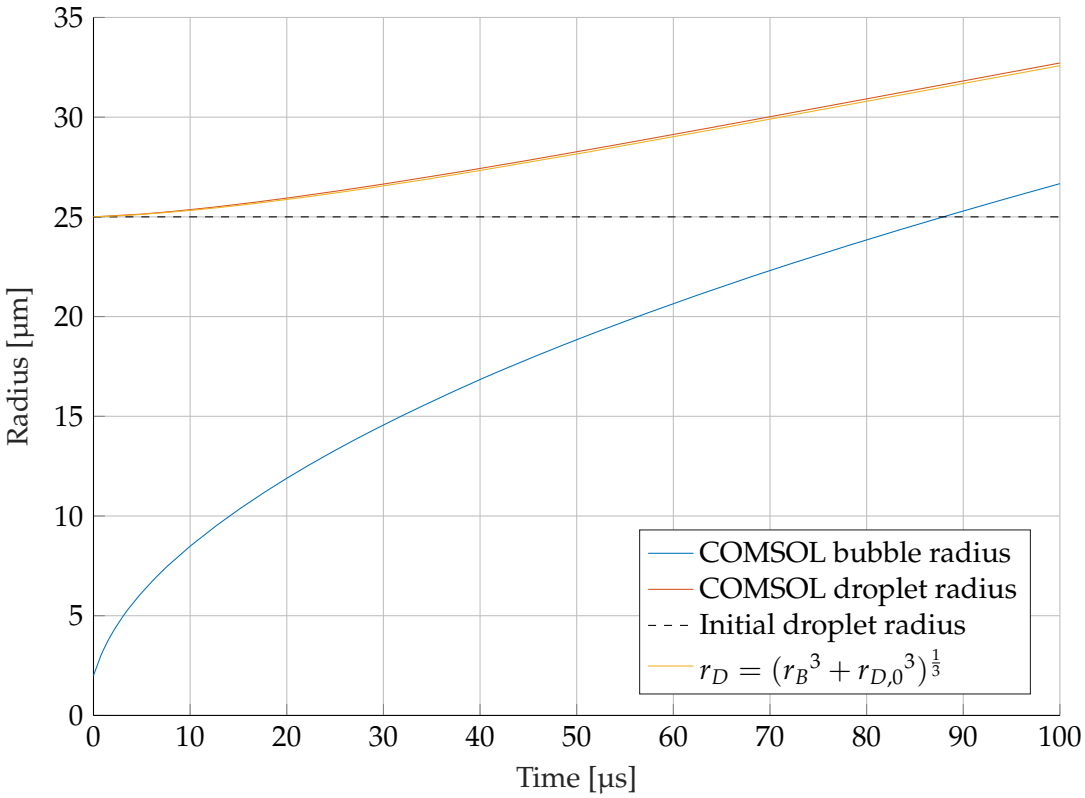

FIGURE 4.6: Plot of the probed droplet radius compared with that calculated from conservation of mass

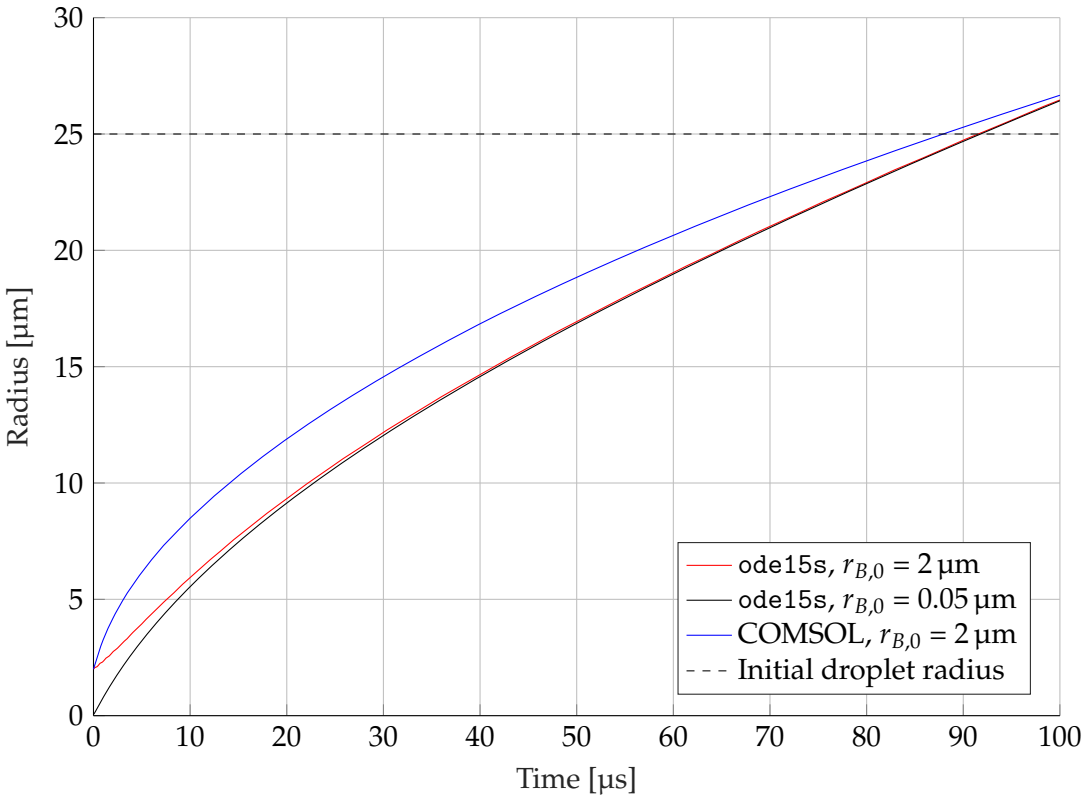

FIGURE 4.7: Plot of radius over time from COMSOL compared with ode15s for concentric cases with different initial conditions.

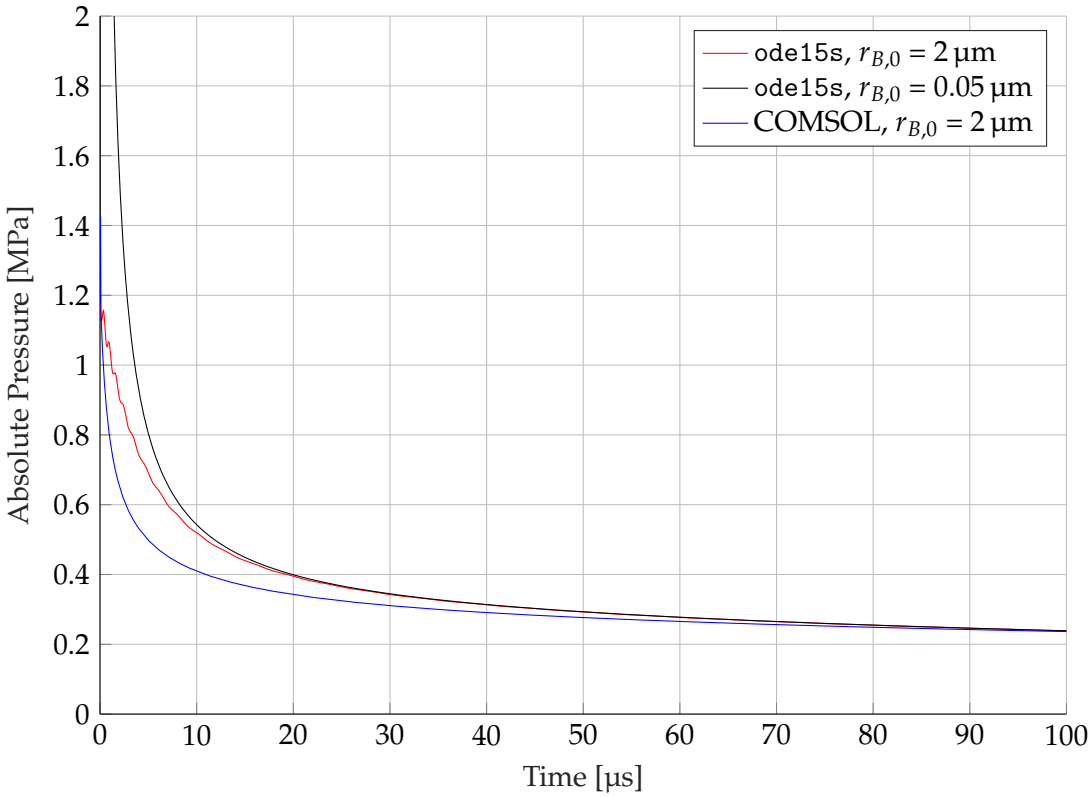

FIGURE 4.8: Plot of pressure over time from COMSOL compared with ode15s for concentric cases with different starting radii

similar relationship as the radius plots can be observed with convergence between different ODE initial conditions. However for COMSOL it can now be seen that the pressure converges with the ODE solution as well, albeit at a slower rate than for the two ODE profiles. This may indicate that the radius plot would also tend towards the same result given more time.

Both of these figures show a clear correlation between the ODE and COMSOL solutions. With the governing equation being highly non-linear it is unsurprising that changing the initial conditions would have a large impact on the result, but as they all appear to converge it gives more confidence in the simplified form of the ODE and that the assumptions made are valid.

4.3.2 Off-Centre Nucleation

Modelling the droplet as 2D axisymmetric also extends to simulating eccentric bubble nucleation for examining how that may affect bubble growth. Figure 4.9 shows surface plots of velocity magnitude at the end of the time period for different initial offsets compared to the concentric case. From these images a clear trend can be observed where the area of the liquid phase at the top of the droplet experiences the largest velocity, with the area becoming more focused and spiking to higher levels as the offset is increased. The eccentric nucleation also exhibits an induced velocity

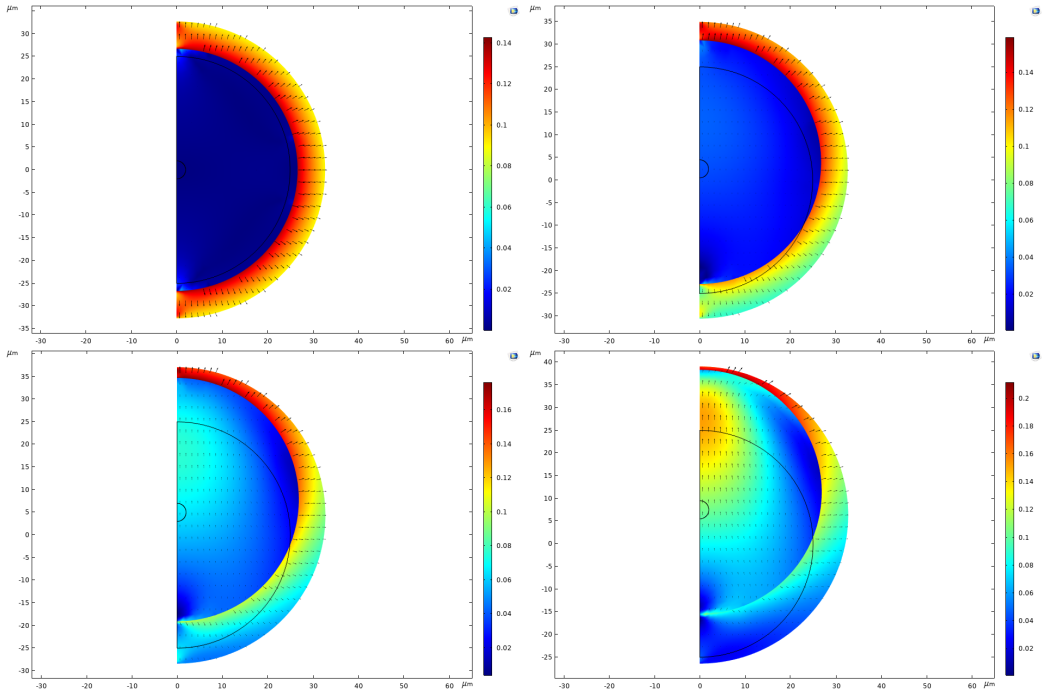

FIGURE 4.9: Surface plots of velocity magnitude at 100 µs for initial offsets of ζ equal to 0.0, 0.1, 0.2, and 0.3 respectively

profile in the bubble whereas in the concentric case the bubble was static. This is presumably a result of the imbalanced velocity in the liquid domain where as the top portion expands more rapidly the bubble must move to fill the void left by the advancing liquid.

Bubble radius for all the different offsets was graphed against time in Figure 4.10 to see if the asymmetry of the liquid surrounding the bubble had any impact on the bubble dynamics. From the ODE, it is expected that a reduced thickness of the liquid phase would impede the bubble growth less, causing the growth rate to increase as seen in Figure 4.9. With larger initial offsets, the average liquid phase thickness around the bubble is reduced and so in theory the more eccentric bubbles may grow faster. The resulting figure instead shows little variance between different offsets with most of the series being visually indistinct but with $\eta = 0.0$ and $\eta = 0.05$ being slightly lower.

An issue that arises from the moving mesh simulation is that as the bubble expands the mesh in the liquid phase compresses which can affect mesh quality in later time steps. In Figure 4.11, surfaces of the mesh skewness for different initial offsets are shown at the end of each simulation. This skewness is a measure of how the cells of elements in the mesh compare to regular shapes with equal interior angles, where a skewness of one corresponds to a regular shape. When the mesh becomes more skewed it can cause problems with accuracy and convergence, especially if inverted cells are generated under high deformations. From the figure, there appears to be good mesh quality for the concentric case in the majority of the domain, but as the

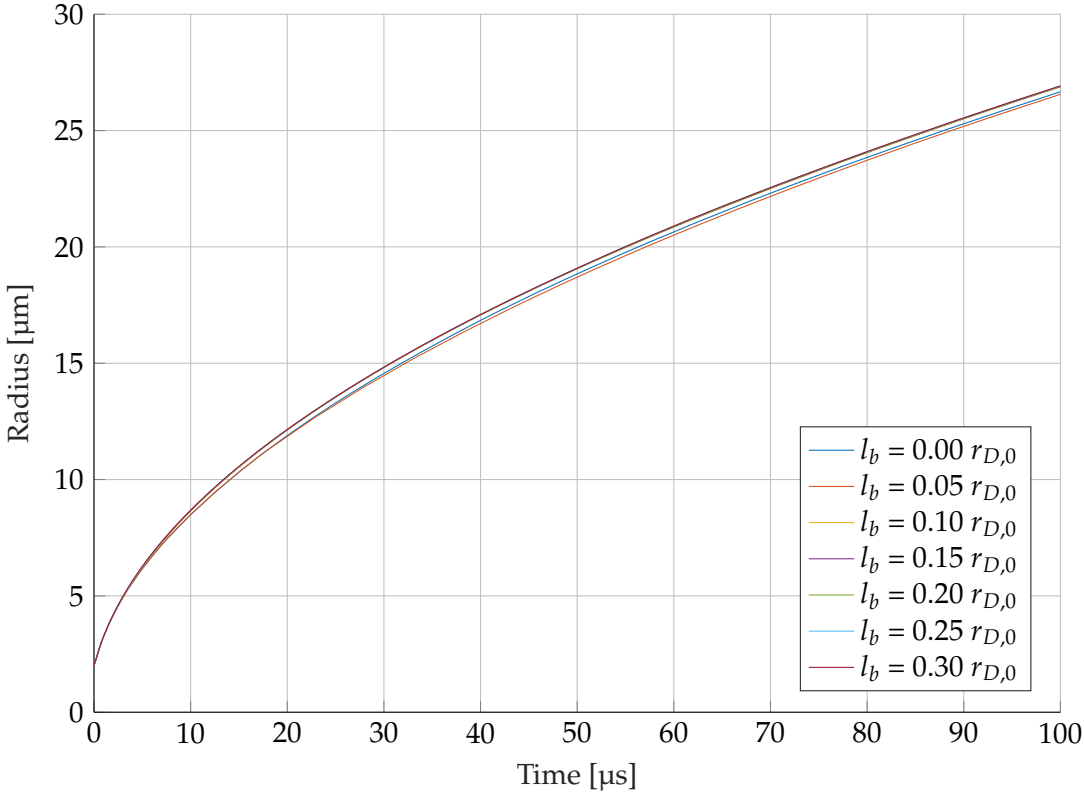

FIGURE 4.10: Plot of bubble radius over time from COMSOL for different initial offsets

nucleation site becomes more concentric, the mesh quality reduces noticeably. This effect is most distinct in the liquid phase domain at the top of the bubble as the asymmetric growth in the liquid phase causes the domain to twist, severely deforming the mesh. Due to the impact mesh quality has on convergence, this may be the cause of failure to resolve higher offsets if the observed trend from the figure continues.

Another aspect of the bubble dynamics to be investigated was the hypothesis that an offset bubble may migrate inward to self centre as a result of some induced pressure profile in the liquid. To track this effect, probes were used to evaluate the location of the centre for the bubble and droplet and then used to calculate ζ according to Equation (4.14) where l_B is the difference between the two centre points. The centre ratio was plotted over time in Figure 4.12 for all the offset simulations. In this graph it can be seen that the centre ratio does tend to decrease over time, with a sharper gradient observed for larger initial offsets. Generally though, the magnitude is not significant enough to reach a near concentric case in a typical time period as the bubble would burst before reaching that state.

The centre ratio is not the only variable to indicate how concentric the bubble is. As an additional measure, the thicknesses of the liquid phase at the top and bottom of the bubble are compared using the ratio γ obtained from Equation (4.19). Plots of

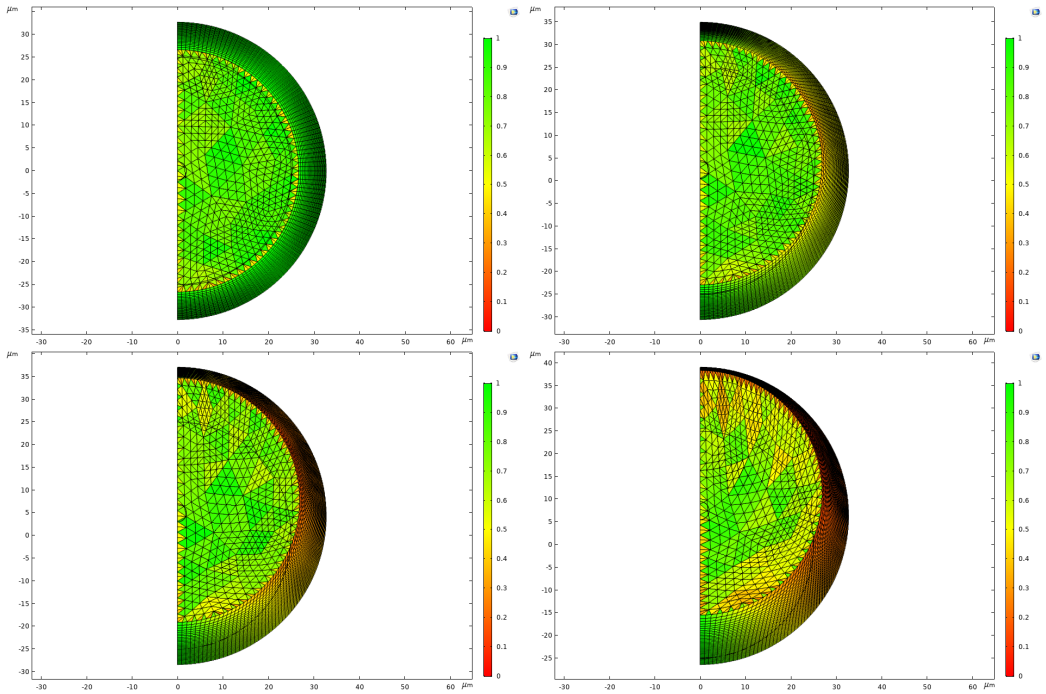

FIGURE 4.11: Plots of mesh quality at 100 µs for initial offsets of ζ equal to 0, 0.1, 0.2, and 0.3 respectively

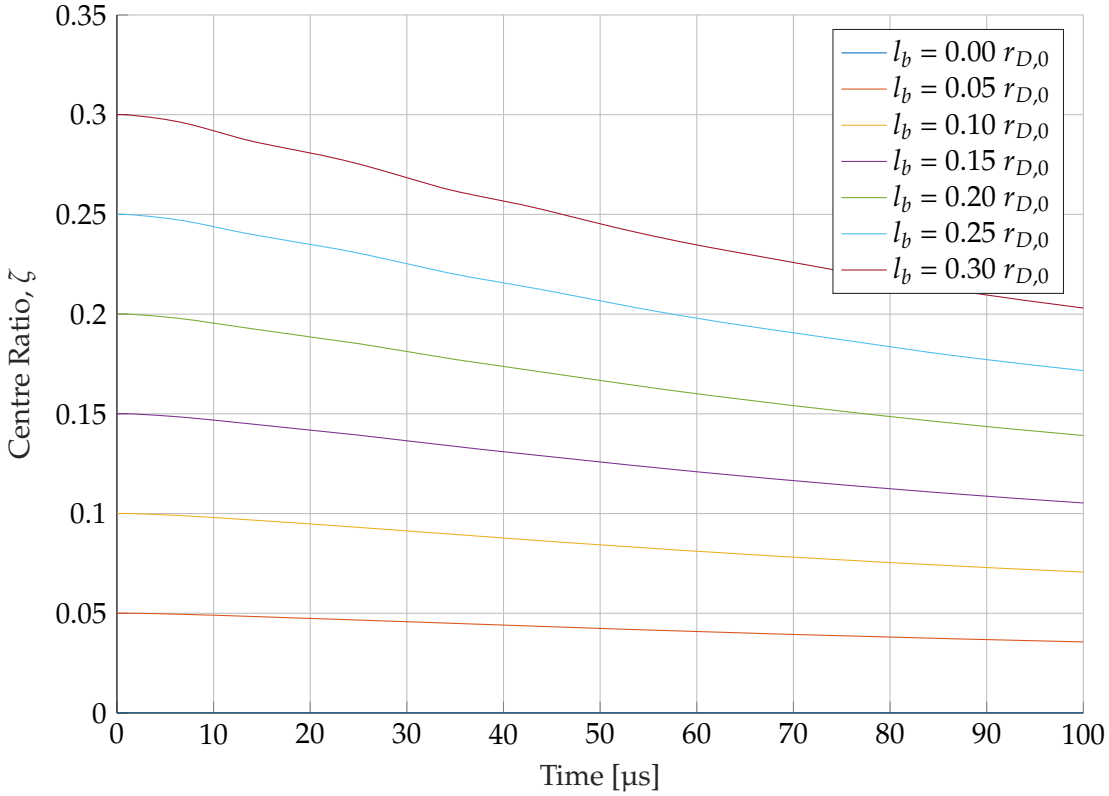

FIGURE 4.12: Plots of the ratio of distance between bubble and droplet centres to initial droplet radius

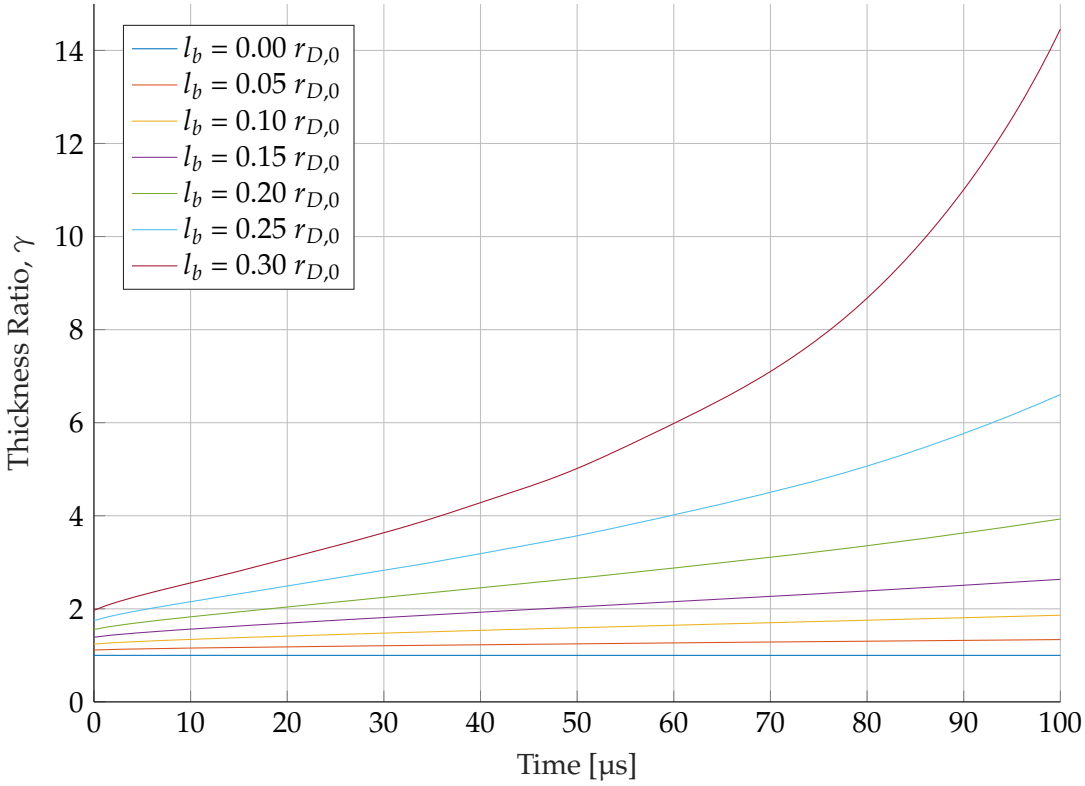

FIGURE 4.13: Plots of the ratio of thickness of the liquid phase between the thickest and thinnest sections.

this ratio over time are displayed in Figure 4.13. For a concentric bubble the thickness ratio should stay at $\gamma = 1$ which indicates that the liquid phase thickness is uniform around θ. In this figure, all the offset series are observed to be increasing over time while the concentric series stays constant as expected. For the highest offsets the trend appears to be exponential and increases at a much faster rate than previous offsets. These results compare favourably with the 2D velocity surfaces in Figure 4.9 as the large discrepancy between the thickness in liquid phase is very noticeable in the image for $\eta = 0.3$. This effect runs counter to the trend of the centre ratio decreasing over time as it instead indicates that the bubble is not becoming more concentric. While there is clearly a movement of the bubble relative to the droplet, its magnitude is too low to move the system towards a concentric state, instead resulting in a squeeze on the liquid phase at the thin boundary.

4.4 Conclusion

Modelling the bubble growth in a droplet with multiple dimensions in COMSOL was used for comparisons with the ODE model, and to investigate the effect of eccentric bubble nucleation. With a 2D axisymmetric component and the Two Phase Flow Moving Mesh module, the system was simulated with initial conditions matching an ODE test case solved using MATLAB. Results of bubble radius and pressure from the 2D solution were plotted against those from the ODE and showed that both

methods converged to the same profile. Applying the same initial conditions from the 2D case to the ODE gave a profile that converged to the standard ODE solution faster than the 2D case but with noticeable oscillatory behaviour. This is due to the Navier-Stokes equations which govern both models being highly non-linear and making the system very dependent on the initial conditions. In addition, this model was used to test the assumption that mass in the liquid phase is conserved and that both the droplet and bubble remain circular. Plotting the conservation of mass expression alongside the probed value of droplet radius showed that they both give the same result. Probes used for calculating the respective domain radii also revealed that with such high surface tension the assumption of circularity in the the ODE was reasonable.

Following this work, the eccentric bubble growth was modelled by shifting the bubble nucleation up the axis of symmetry by a range of offset lengths. This came with computational challenges as the dynamics of the system coupled with the moving mesh caused the overall element quality to go down. Despite some larger offsets having convergence issue, it was found that the growth of the bubble was mostly unaffected by the asymmetry in the liquid phase. There was also some movement of the bubble towards the centre of the droplet which increased with offset lengths. This was however countered by more severe compression of the liquid phase at the top side which would lead to bursting of the droplet sooner than would occur for a concentric case.

Chapter 5

Interfacial and Diffusive Transport

5.1 Introduction

In Wainwright et al. (2019) the proposed mechanisms for bubble growth involves the diffusion of monatomic nitrogen through solution to the bubble interface, where it is adsorbed and then desorbed through the boundary. This process is thought to be rate limited by one of these mechanisms, such that the total rate of accumulation for nitrogen in the bubble is dependent on whichever mechanism is slower. Different expressions for calculating the rates of molar accumulation were generated and compared with data from the experimental recordings. The aim of this chapter is to assess which of the proposed mechanisms best fits the observed events in radius profile and whether the parameter values required are reasonable physically.

5.2 Methods

A more detailed investigation requires looking at the concentration profile throughout the liquid phase. Diffusion of chemical species in the liquid phase follows Fick's second law of diffusion which in spherical coordinates takes the form

$$\frac{\partial c}{\partial t} = D\frac{1}{r^2}\frac{\partial}{\partial r}\left(r^2\frac{\partial c}{\partial r}\right) \tag{5.1}$$

where c is the concentration of nitrogen in the liquid phase in $\mathrm{mol\,m^{-3}}$ and D is the diffusion coefficient for nitrogen in the Al:Zr:O:N solution with units of $\mathrm{m^2\,s^{-1}}$. This is expanded out using the product rule to give

$$\frac{\partial c}{\partial t} = D\left(\frac{\partial^2 c}{\partial r^2} + \frac{2}{r}\frac{\partial c}{\partial r}\right) \tag{5.2}$$

Coupling this partial differential equation with the bubble growth ODE becomes simpler when applying a coordinate transform. This makes the spatial discretisation a constant interval instead of moving boundary points. To achieve an interval of zero

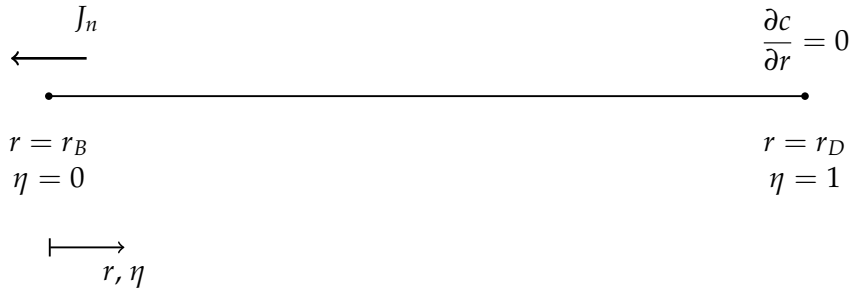

FIGURE 5.1: Spatial domain of liquid phase for solving Fick's Second Law with boundary conditions

to one, the coordinate transform is defined as

$$\eta = \frac{r - r_B}{r_D - r_B} \tag{5.3}$$

which when differentiated with respect to radius gives

$$\frac{d\eta}{dr} = \frac{1}{r_D - r_B} \tag{5.4}$$

These equations can be rearranged to substitute into the original diffusion equation such that

$$r = \eta \left(r_D - r_B\right) + r_B \tag{5.5}$$

and the gradient of concentration with respect to radius is expressed in terms of the derivative of η as

$$\frac{\partial c}{\partial r} = \frac{\partial c}{\partial \eta} \frac{d\eta}{dr} \tag{5.6}$$

The governing equation can be changed to the new coordinate system by substituting Equations (5.5) and (5.6) into Equation (5.2). Doing so results in the transformed equation of

$$\frac{\partial c}{\partial t} = D \left(\frac{1}{\left(r_D - r_B\right)^2} \frac{\partial^2 c}{\partial \eta^2} + \frac{2}{\left(\eta \left(r_D - r_B\right) + r_B\right)\left(r_D - r_B\right)} \frac{\partial c}{\partial \eta} \right) \tag{5.7}$$

The domain used for this problem is one dimensional and ranges from the bubble interface at $r = r_B$ to the droplet surface at $r = r_D$. The boundary condition for the outer droplet radius was defined as a Neumann condition of zero flux. This comes from the assumption that no nitrogen from the atmosphere is absorbed into the droplet during bubble growth and all nitrogen in solution only leaves through the bubble interface.

An illustration of the computational domain is provided in Figure 5.1. In this diagram, J_n is the flux of nitrogen from the liquid phase entering the bubble which couples with the bubble growth ODE from Equation (2.9), whereby the number of

moles of nitrogen in the bubble is calculated as before with

$$n(t) = \int_0^t J_n 4\pi {r_B}^2 dt + n_0 \tag{5.8}$$

The flux is calculated from the concentration in the liquid phase which varies depending on the boundary condition chosen. For the bubble interface, a number of different conditions were trialled and compared with one another. Firstly, a Dirichlet condition of zero concentration at the bubble interface was used where

$$c(\eta = 0) = 0\,\mathrm{mol\,m^{-3}} \tag{5.9}$$

which arises from an assumption that the rate of adsorption across the interface is so much higher than the flux through the liquid phase that all molecules that reach the interface are immediately adsorbed, and as such require that growth is rate limited by diffusion. As a result, the flux of nitrogen into the bubble is calculated using the concentration gradient at the bubble interface with

$$J_n = \frac{D}{r_D - r_B} \frac{\partial c}{\partial \eta}\Big|_{\eta=0} \tag{5.10}$$

The second condition was a Robin boundary where flux is proportional to the difference in concentration between the bubble and the node at the interface, leading to

$$\frac{D}{r_D - r_B} \frac{\partial c}{\partial \eta}\Big|_{\eta=0} = h\left(c(\eta = 0) - c_B\right) \tag{5.11}$$

and so with the definition from Equation (5.10) gives

$$J_n = h\left(c(\eta = 0) - c_B\right) \tag{5.12}$$

where h is the mass transfer coefficient of adsorption across the bubble interface with units of $\mathrm{m\,s^{-1}}$ and c_B is the concentration of nitrogen in the bubble as $c_B = \frac{n(t)}{V_B}$. In this way, the approach combines the different mechanisms and links them together, allowing the relative effect of each process on the system to be altered by adjusting the different coefficients.

Finally, a Neumann condition was applied to match the flux from the event analysis to see how the concentration profile evolves when using the scheme best fitting the experimental data. Applying this to Event 1 for the linearly proportional radius results in defining the flux as

$$J_n = \frac{D}{r_D - r_B} \frac{\partial c}{\partial \eta}\Big|_{\eta=0} = \frac{\dot{N}_1 r_B}{A_B} \tag{5.13}$$

so that when substituted into Equation (5.8) results in the same flux as the events,

however with the difference that it is integrated over time instead of being multiplied by the time elapsed as was previously done in Equation (2.15). While this discrepancy needs to be accounted for, the boundary condition shows the evolution of concentration for bubble growth for a defined flux. This was done to serve as a comparison for the solutions from other boundary conditions against what best agrees with experiments.

Solving this problem requires the use of the Crank-Nicolson method as it is an efficient way to solve the diffusion equation. As a mix of the Backward and Forward Euler approximations it uses values from the new and previous time step, making it an implicit solver. Applying finite difference discretisations to Equation (5.7) according to the Crank-Nicolson method gives

$$\frac{c_i^{j+1}-c_i^j}{\Delta t}=\frac{D}{2}\left(\frac{1}{\left(r_D-r_B\right)^2}\frac{c_{i-1}^{j+1}-2c_i^{j+1}+c_{i+1}^{j+1}}{\Delta\eta^2}+\frac{2}{\left(\eta\left(r_D-r_B\right)+r_B\right)\left(r_D-r_B\right)}\frac{c_{i+1}^{j+1}-c_{i-1}^{j+1}}{2\Delta\eta}\right.$$
$$\left.+\frac{1}{\left(r_D-r_B\right)^2}\frac{c_{i-1}^{j}-2c_i^{j}+c_{i+1}^{j}}{\Delta\eta^2}+\frac{2}{\left(\eta\left(r_D-r_B\right)+r_B\right)\left(r_D-r_B\right)}\frac{c_{i+1}^{j}-c_{i-1}^{j}}{2\Delta\eta}\right) \quad (5.14)$$

where the i subscript indicates the spatial node for $i = 1, 2, \ldots, n$ with n being the total number of nodes and where $i = 1$ at $\eta = 0$ and $i = n$ at $\eta = 1$. With a uniform distribution of nodes, the change of η is calculated with

$$\Delta\eta=\frac{\eta(r_D)-\eta(r_B)}{n-1}=\frac{1}{n-1} \quad (5.15)$$

and for the temporal index of j starting with $t = 0$ at $j = 1$ the change of time is calculated using

$$\Delta t=t^{j+1}-t^j \quad (5.16)$$

To solve for the concentration profile Equation (5.14) is rearranged into matrix form with terms of the $j+1$ concentrations on the L.H.S and terms of j on the R.H.S. Firstly, the following coefficient substitutions are made for

$$\lambda_1=\frac{D\Delta t}{2\Delta\eta^2\left(r_D-r_B\right)^2} \quad (5.17)$$

and

$$\lambda_2=\frac{D\Delta t}{2\Delta\eta\left(\eta\left(r_D-r_B\right)+r_B\right)\left(r_D-r_B\right)} \quad (5.18)$$

which allows the rearranged equation to simplify to

$$\left(-\lambda_1+\lambda_2\right)c_{i-1}^{j+1}+\left(1+2\lambda_1\right)c_i^{j+1}+\left(-\lambda_1-\lambda_2\right)c_{i+1}^{j+1}$$
$$=\left(\lambda_1-\lambda_2\right)c_{i-1}^{j}+\left(1-2\lambda_1\right)c_i^{j}+\left(\lambda_1+\lambda_2\right)c_{i+1}^{j} \quad (5.19)$$

For the boundary condition at the droplet surface, the zero flux Neumann condition with the equation

$$D\frac{\partial c}{\partial r} = 0 \tag{5.20}$$

which with the implementation of a ghost node at $i = n + 1$ discretises to

$$\frac{D}{r_D - r_B}\frac{c_{i+1} - c_{i-1}}{2\Delta\eta} = 0 \tag{5.21}$$

which results in a substitution of $c_{i+1} = c_{i-1}$ into the discretised PDE of Equation (5.19) for the node on the boundary where $i = n$ to obtain the boundary equation of

$$-2\lambda_1 c_{n-1}^{j+1} + (1 + 2\lambda_1)\, c_n^{j+1} = 2\lambda_1 c_{n-1}^{j} + (1 - 2\lambda_1)\, c_n^{j} \tag{5.22}$$

In a similar manner, the equation for the Robin boundary condition from (5.12) is discretised to get

$$\frac{D}{r_D - r_B}\frac{c_{i+1} - c_{i-1}}{2\Delta\eta} = h\,(c_i - c_B) \tag{5.23}$$

and so when applied to the bubble interface where $i = 1$ this rearranges to

$$c_0 = c_2 - \frac{2h\Delta\eta\,(r_D - r_B)}{D}\,(c_1 - c_B) \tag{5.24}$$

leading to a new simplified coefficient term of

$$\lambda_3 = \frac{2h\Delta\eta}{D}(r_D - r_B)(\lambda_1 - \lambda_2) = \frac{h\Delta t}{\Delta\eta(r_D - r_B)} - \frac{h\Delta t}{\eta(r_D - r_B) + r_B} \tag{5.25}$$

which then substitutes into the full discretised equation to give the other boundary equation of

$$(1 + 2\lambda_1 + \lambda_3)\, c_1^{j+1} - 2\lambda_1 c_2^{j+1} = (1 - 2\lambda_1 - \lambda_3)\, c_1^{j} + 2\lambda_1 c_2^{j} + 2\lambda_3 c_B^{j} \tag{5.26}$$

For the Neumann condition on the bubble interface Equation (5.13) discretises to

$$\frac{D}{r_D - r_B}\frac{c_{i+1} - c_{i-1}}{2\Delta\eta} = \frac{\dot{N}_1}{4\pi r_B} \tag{5.27}$$

and as before results in the boundary equation of the form

$$(1 + 2\lambda_1)\, c_1^{j+1} - 2\lambda_1 c_2^{j+1} = (1 - 2\lambda_1)\, c_1^{j} + 2\lambda_1 c_2^{j} - \frac{\dot{N}_1\Delta\eta(r_D - r_B)}{D\pi r_B}(\lambda_1 - \lambda_2) \tag{5.28}$$

The Dirichlet condition when discretised at the boundary simply becomes

$$c_1 = 0 \tag{5.29}$$

which is then the entire equation applied to the boundary node.

With all the necessary equations derived, the system can be solved by converting to a matrix form of

$$\boldsymbol{A}\vec{c} = \vec{b} \tag{5.30}$$

where $\boldsymbol{A}$ is an $n \times n$ matrix that contains the coefficients of the c terms in the i^{th} row for the equation at the corresponding node and all entries outside the tri-diagonal lines are zero. With the Robin condition on the first row and zero flux Neumann on the last this gives

$$\boldsymbol{A} = \begin{bmatrix} 1+2\lambda_1+\lambda_3 & -2\lambda_1 & 0 & \cdots & \\ -\lambda_1+\lambda_2 & 1+2\lambda_1 & -\lambda_1-\lambda_2 & 0 & \cdots \\ & \ddots & \ddots & \ddots & \\ \cdots & 0 & -\lambda_1+\lambda_2 & 1+2\lambda_1 & -\lambda_1-\lambda_2 \\ & \cdots & 0 & -2\lambda_1 & 1+2\lambda_1 \end{bmatrix}$$

The $\vec{c}$ array is simply an $n \times 1$ vector containing the values of concentration at the i^{th} node in the same row for the new time step at $j+1$ to get

$$\vec{c} = \begin{bmatrix} c_1^{j+1} \\ c_2^{j+1} \\ \vdots \\ c_n^{j+1} \end{bmatrix}$$

And finally the $\vec{b}$ array contains all the terms on the right hand side of the discretised equations consisting of forcing terms and sums of concentrations at the previous time step so with the Robin condition results in the array

$$\vec{b} = \begin{bmatrix} (\lambda_1-\lambda_2-\lambda_3)\,c_1^j + 2\lambda_1 c_2^j + 2\lambda_3 c_B \\ (\lambda_1-\lambda_2)\,c_1^j + (1-2\lambda_1)\,c_2^j + (\lambda_1+\lambda_2)\,c_3^j \\ \vdots \\ (\lambda_1-\lambda_2)\,c_{i-1}^j + (1-2\lambda_1)\,c_i^j + (\lambda_1+\lambda_2)\,c_{i+1}^j \\ \vdots \\ (\lambda_1-\lambda_2)\,c_{n-2}^j + (1-2\lambda_1)\,c_{n-1}^j + (\lambda_1+\lambda_2)\,c_n^j \\ -2\lambda_1 c_{n-1}^j + (1+2\lambda_1)c_n^j \end{bmatrix}$$

The whole system was solved by iterating the solution of $\vec{c} = \boldsymbol{A}\backslash\vec{b}$ over time from t=0 µs to $t = t_{max}$ in steps of 0.01 µs with $t_{max} = 25$ µs. The spatial domain was split into $n = 1001$ equally spaced nodes as a compromise between providing sufficient detail and minimising computation time. Lower numbers of nodes were too coarse to accurately calculate the concentration profile whereas increased nodes lead to prohibitively long solution times. Within each iteration, the Crank-Nicolson method was applied first and from the new values of concentration the amount of nitrogen in the bubble was calculated with Equation (5.8) through numeric integration and

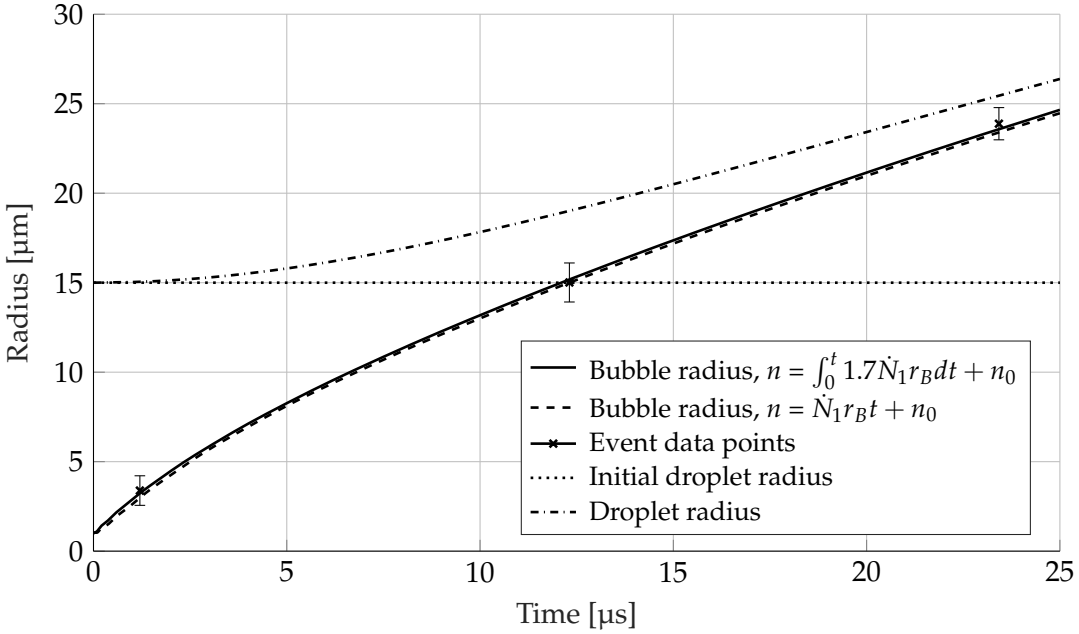

FIGURE 5.2: Bubble radius profile for the Neumann boundary condition compared to data from Event 1.

input to `ode15s`, solving the bubble growth ODE for the period from t^j to t^{j+1} where the initial values used were r_B and q at $t = t^j$. Then the new values of r_B and q are saved for $t = t^{j+1}$ and the iteration progresses to the next time step. By performing the iterations this way, the coupled solution is generated implicitly as growth is determined by concentration values from the next time step which has the benefit of increasing the area of stability for the solution. Even so, the time step must be kept small enough to avoid large jumps in output that may result in convergence issues. For each boundary case, the values of initial concentration, diffusion coefficient, and mass transfer coefficient were found manually to try and obtain the nearest agreement with experimental results from Event 1.

5.3 Results & Discussion

By specifying the flux for the Neumann condition as $J_n = \frac{\dot{N}_1 r_B}{A_B}$, plots of bubble radius and concentration were generated and are shown in Figures 5.2 and 5.3 respectively. Data points from Event 1 are plotted alongside radius, as well as the scheme for $\dot{N}_1$. By integrating the term of $\dot{N}_1 r_B$, the magnitude of growth is reduced. This is compensated by multiplying this value by a factor of 1.7 which was found by comparing the result of integrating $\dot{N}_1 r_B$ with the number of moles calculated using Equation (2.15) for the first order scheme. It can be seen in the figure that the two profiles of radius are extremely close after this correction, indicating that the integration of the scheme returns the same shape profile and would imply that for $\int_0^t \dot{N}_1 r_B dt = \frac{1}{1.7}\dot{N}_1 r_B t$.

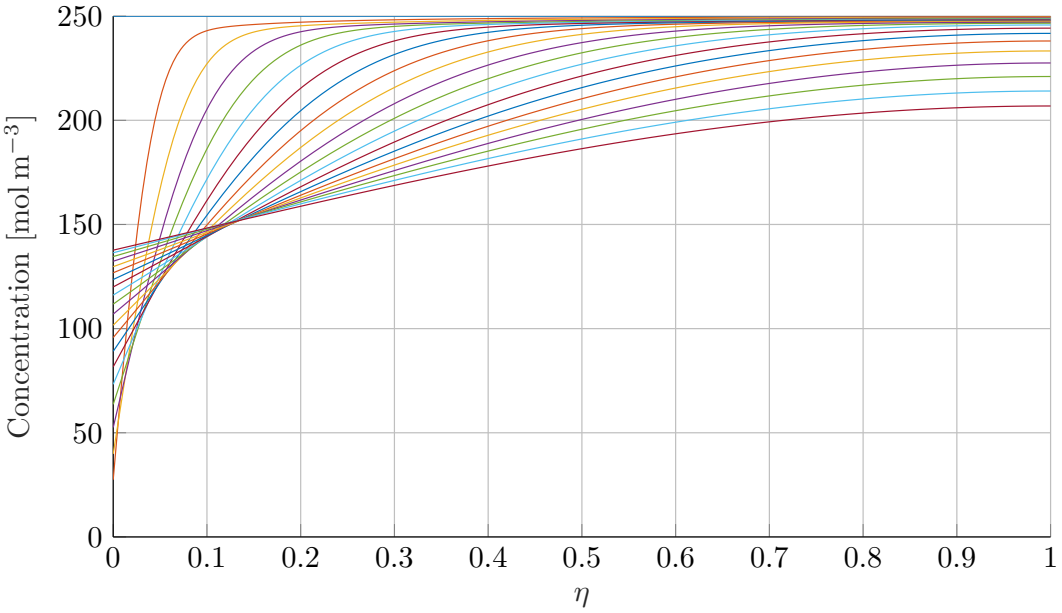

FIGURE 5.3: Concentration profiles for the Neumann boundary condition over time.

The concentration profiles were calculated from an initial concentration of $c_0 = 250\,\mathrm{mol\,m^{-3}}$ and with a diffusion coefficient of $D = 1 \times 10^{-7}\,\mathrm{m^2\,s^{-1}}$. In the figure, these profiles were plotted for every 125 time steps for clarity. This shows a large initial flux over the boundary that reduces as time progresses which is counteracted by the area of the bubble increasing, so that the total rate of nitrogen flowing into the bubble remains linearly proportional to bubble radius. As the bubble and droplet expands, the domain for diffusion shrinks. The smaller domain causes more rapid changes in concentration as the gradients in η have a factor of $\frac{1}{r_D - r_B}$. This is presented by the overall difference in concentration between the interface getting smaller and more evenly distributed, as compared to the sharp dip in the first time step.

Moving to the Dirchlet boundary condition of $c_0 = 0$, the solutions for bubble growth and concentration are now linked. Figure 5.4 shows a plot of the resulting bubble radius again compared with data from Event 1, including the linearly proportional molar flow scheme. This solution was computed with a value of $c_0 = 250\,\mathrm{mol\,m^{-3}}$ like the Neumann case, but with a reduced diffusion coefficient of $D = 0.4 \times 10^{-7}\,\mathrm{m^2\,s^{-1}}$. The radius profile shown has limited agreement with the data as it features an increasing growth rate for these values.

Concentration profiles for the Dirichlet condition are shown in Figure 5.5. With the concentration at the boundary constrained to zero there is no increasing concentration like for the Neumann condition. The flux into the bubble as calculated through the gradient at the boundary which is decreasing over time, however not to the same extent as the Neumann profiles which is causing the growth rate of the bubble to rise over time.

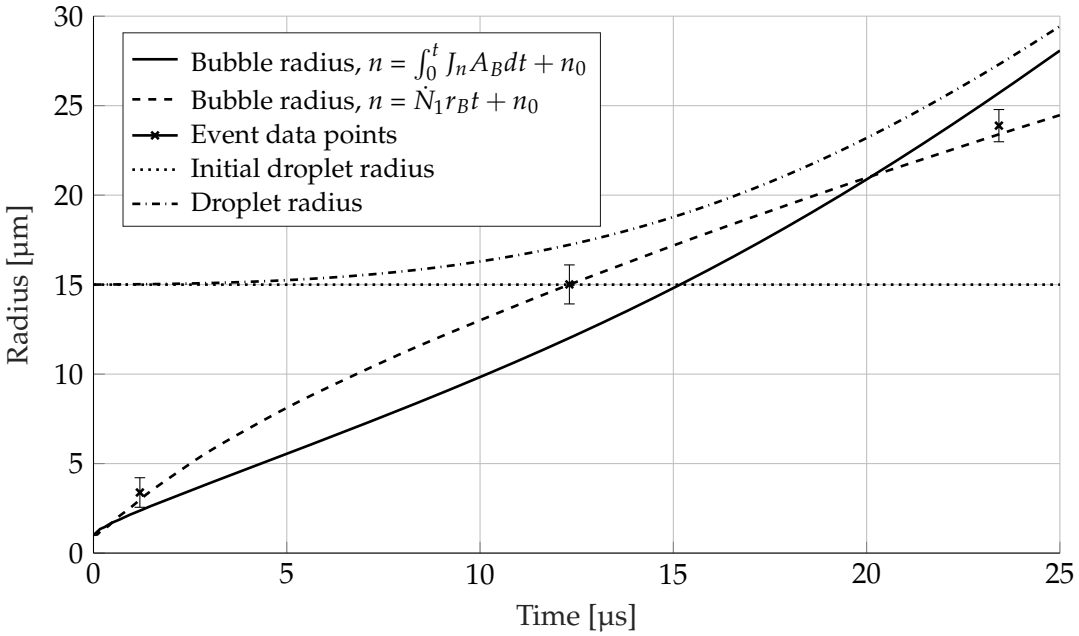

FIGURE 5.4: Bubble radius profile for the Dirichlet boundary condition compared to data from Event 1.

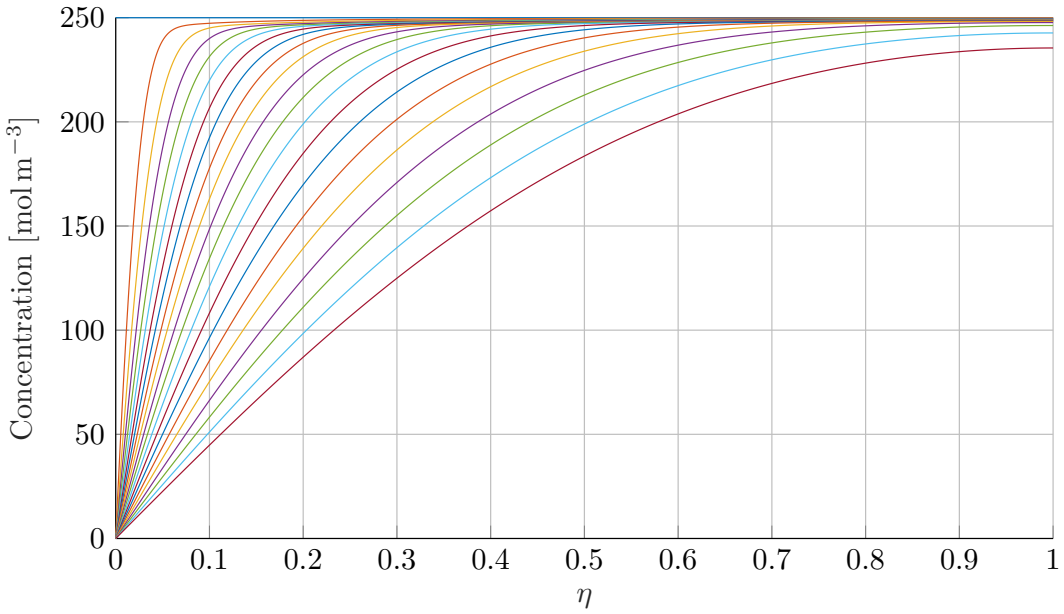

FIGURE 5.5: Concentration profiles for the Dirichlet boundary condition over time.

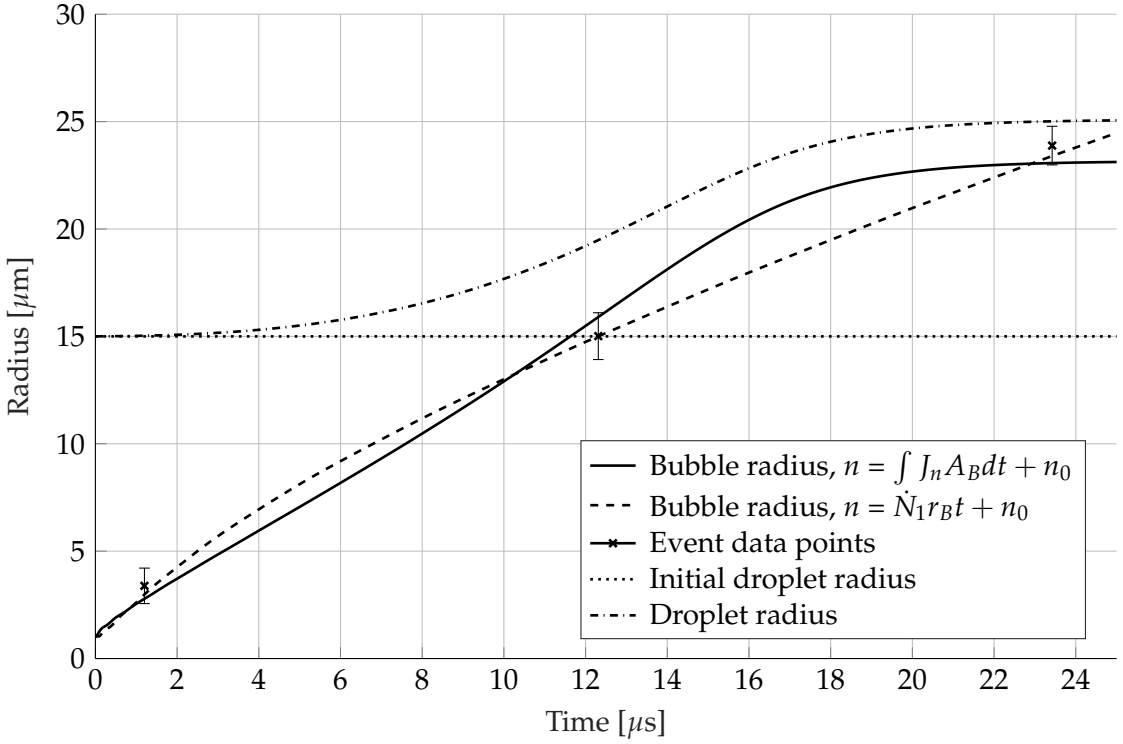

FIGURE 5.6: Bubble radius profile for the Dirichlet boundary condition compared to data from Event 1 with increased diffusion and less initial concentration.

By increasing the diffusion coefficient to $D = 8 \times 10^{-7}\,\mathrm{m^2\,s^{-1}}$ and lowering initial concentration to $c_0 = 55\,\mathrm{mol\,m^{-3}}$, the Dirichlet system was solved to produce the bubble radius for Figure 5.6 and concentration profiles for Figure 5.7. These values give a radius plot that lies within uncertainty limits for all data points. Despite this, the profile appears strange as the radius is increasing until just before the last data point where it appears to level off. Inspecting the concentration plot reveals that at the later time steps the liquid phase has been severely depleted of nitrogen, resulting in a much lower flux to the bubble.

Compared to the other plot of concentration for the Dirichlet condition, these profiles have a wider variance in gradients which enables the solution to tend toward the data points. As the concentration goes to zero however, there is no longer any more impetus on the bubble to grow after the last time step. For the event, the reaction does not stop after the last frame, but continues to grow before breaking apart. As a result, it does not seem likely that the Dirichlet condition is suitable for modelling diffusion as it does not allow for further growth toward microexplosion outside the three frames of data.

The system was then solved with a Robin condition with values of $c_0 = 250\,\mathrm{mol\,m^{-3}}$ and $D = 2 \times 10^{-7}\,\mathrm{m^2\,s^{-1}}$, but now with the addition of the adsorption transfer coefficient with a value of $h = 0.2\,\mathrm{m\,s^{-1}}$. The solution for bubble radius in this case is plotted in Figure 5.8 which shows the gradient of the radius increasing over time.

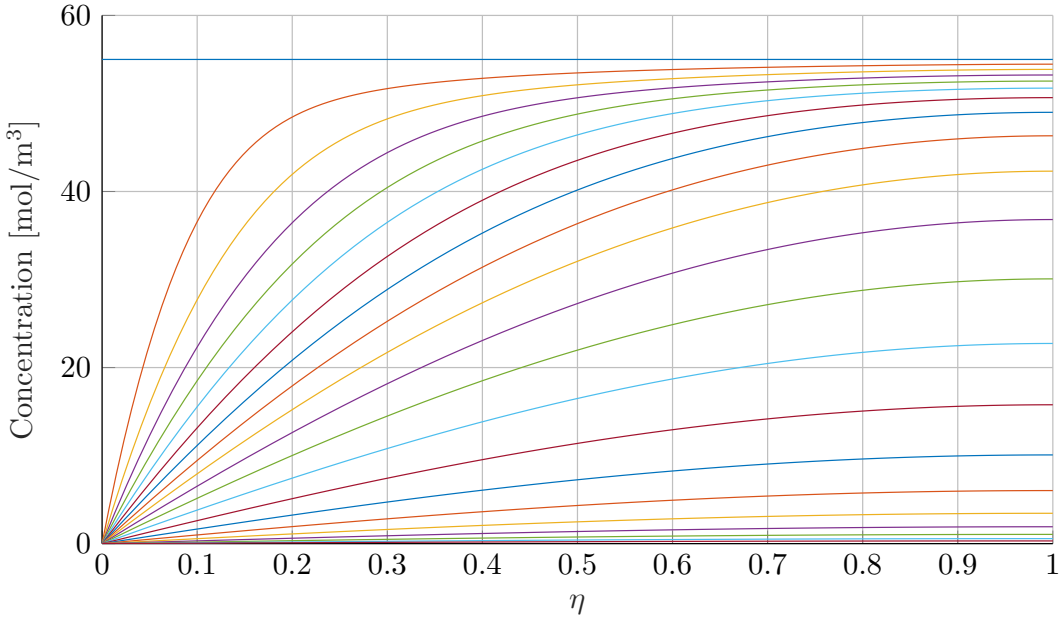

FIGURE 5.7: Concentration profiles for the Dirichlet boundary condition over time with increased diffusion and less initial concentration.

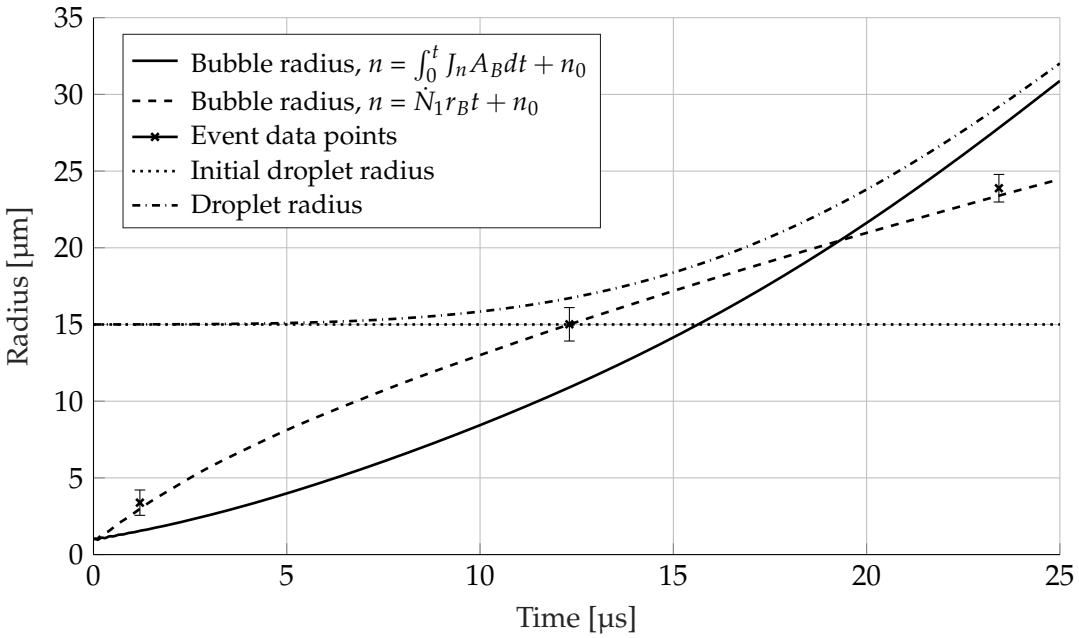

FIGURE 5.8: Bubble radius profile for the Robin boundary condition compared to data from Event 1.

This does not provide a strong fit with data as the rate of increase is higher than the first Dirichlet case.

Inspecting Figure 5.9, which shows concentration profiles for the Robin condition, reveals that the gradient at the bubble interface is reducing too slowly. Compared with the Neumann concentration, it also does not feature a rise of concentration at the interface where the flow into the bubble becomes less than flow from diffusion in

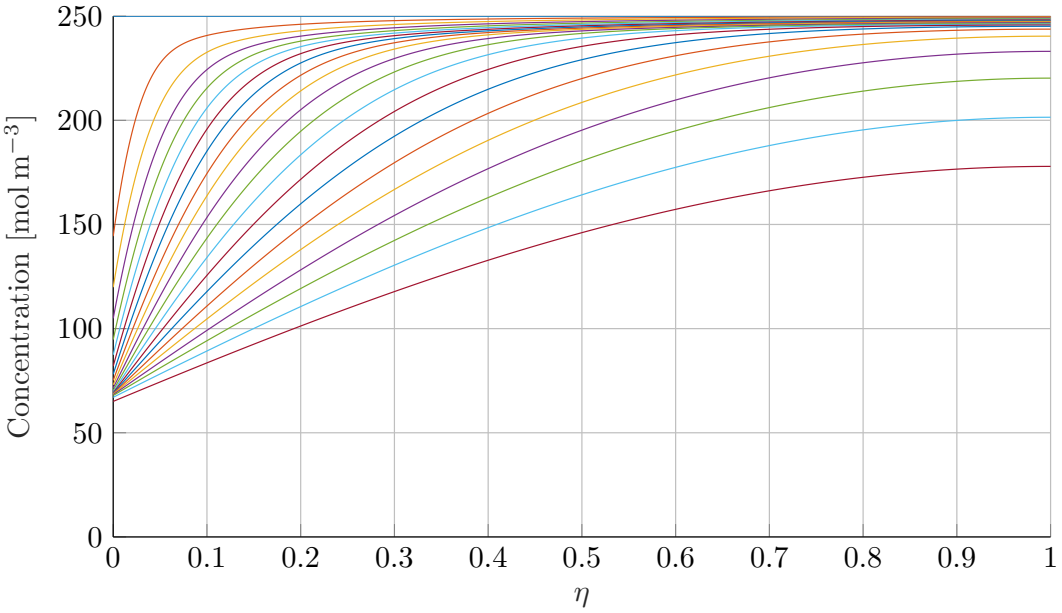

FIGURE 5.9: Concentration profiles for the Robin boundary condition over time.

the rest of the liquid, instead appearing more similar to the Dirichlet profiles. Looking at the boundary condition itself, the flux is calculated as the difference between concentration at the interface and in the bubble. The bubble concentration is decreasing over time as the volume increases faster than the amount of nitrogen, meaning the concentration at the interface has to decrease as well to correspond with the flux reducing.

For this expression of flux, the Robin condition does not adequately match the data despite having more potential to be similar to the Neumann solution than the Dirichlet condition. Future work would involve exploring other functions for flux of $J_n = f(c, r_B, t)$ that result in a scheme matching the Neumann solution. One possibility could be to use the absolute difference in moles rather than concentration, or using values from the bulk of the liquid rather than just at the interface. The act of coupling bubble growth with diffusion makes finding the right expression challenging as opposed to the Neumann condition where the flux is defined independently from concentration, the coupled solution can result in feedback loops of growth that cause oscillations or erratic changes in flux.

Another possible approach is to explore formulations of interface adsorption in more detail. The mathematical expressions for the transport across the interface are simplistic and fail to account for factors such as size and time which may affect the flux across the interface. Using the underlying knowledge from the physics may aid in obtaining a Robin condition with stronger agreement with the event analysis.

The diffusion coefficient of nitrogen in the Al:Zr:O:N solution is not known explicitly and is chosen to fit the solution to the data. While it has not been calculated

experimentally, other researchers have derived diffusion coefficients such as Inouye et al. (1973), Yang et al. (2014), and Sacris and Parlee (1970). In these papers values of the coefficient range from $D = 0.82 \times 10^{-9}\ \mathrm{m^2\,s^{-1}}$ for nitrogen in liquid iron to $D = 4.134 \times 10^{-6}\ \mathrm{m^2\,s^{-1}}$ for hydrogen in liquid silver. These values show that diffusion in these simulations has been chosen within a similar range as to what would be expected for nitrogen in the Al:Zr:O:N solution of this system.

With the assumption that there is no flux of nitrogen into the liquid phase, the initial concentration must be sufficient to grow the bubble to the point of microexplosion. From the Neumann simulation, the initial concentration of $250\,\mathrm{mol\,m^{-3}}$ corresponds to an amount of 3.5332×10^{-12} mol of nitrogen in the liquid phase. At the final time step, there is 6.9823×10^{-13} mol within the bubble corresponding to 19.8% of the initial amount in the solution. This amount therefore provides a sufficient supply of nitrogen to continue growing the bubble towards a microexplosion. For the Al:Zr composite at 1:1 atomic ratio, the metal atoms have an average molar volume of $12\,\mathrm{m^3\,mol^{-1}}$ which divides the volume liquid to give the moles of metal in solution as 1.1781×10^{-9} mol. This means that the initial amount of nitrogen in solution would be 0.3% of the total amount of atomic matter, neglecting the presence of oxygen and assuming the nitrogen does not displace any of the metal atoms from the liquid phase. This corresponds to around 0.07 wt.% of nitrogen. In Paek et al. (2013) nitrogen was observed in iron alloys as high as 0.0933 wt.% at a lower temperature. This indicates that achieving a sufficient level of nitrogen in the liquid is reasonable despite the true solubility of nitrogen in the Al:Zr alloy solution being unknown .

5.4 Conclusion

This chapter explores the behaviour of the chemical species in the liquid phase of the droplet and how they interact with the bubble growth dynamics. To do this the domain was modelled with Fick's second law of diffusion applied to concentration of nitrogen in the solution. The resulting partial differential equation was adjusted with a coordinate transform so it could be coupled with the bubble growth ODE. From there different boundary conditions were applied at the bubble interface to see which condition resulted in a bubble radius profile that fitted with data points from the experiments. Of the different conditions applied, the Robin and Dirichlet conditions used the values of concentration at the boundary to calculate flux into the bubble. The Neumann condition instead calculated the reaction of the concentration to an independent flux expression that was evaluated in the bubble event analysis for Event 1. While the Dirichlet condition parameters could be found to fit within uncertainty limits on the data, neither it nor the proposed Robin condition were found to be accurately describing the flow of nitrogen into the bubble due to high errors, or with a non-physical concentration. With the Neumann condition and an estimated value of diffusion coefficient, the resulting concentration profiles were found to require a minimum of $250\,\mathrm{mol\,m^{-3}}$ initial concentration for the bubble to

grow to match Event 1 data. This result is a reasonable limit as it corresponds to around 0.3% by atom of the initial solution, and so is theoretically a likely situation for any given particle to achieve miroexplosions.

Chapter 6

Conclusions

This thesis contains the investigation and simulation of bubble growth within burning metal droplets that lead to microexplosions. Metal powders are commonly used as an energetic additive to combustion processes where microexplosions may allow for more desirable burn characteristics. To better understand this process, the system was modelled for a 1:1 atomic ratio Al:Zr powder in one dimension with an axisymmetric assumption, allowing the governing r-component of the Navier-Stokes equations to be reduced to an ordinary differential equation with the bubble radius as the dependent variable. The resultant ODE is of second order and so was decomposed into two first order ODEs to allow it to be solved using numerical methods. Growth of the bubble was theorised to be caused by nitrogen coming out of the Al:Zr:O:N solution as it was displaced by the more stable oxygen from atmosphere and then desorbing into the bubble. As a first step, the growth was driven by pressure in the bubble calculated from the ideal gas law with different expressions of $n(t)$, the number of moles of nitrogen in the bubble. It was found that the system was nonlinear and stiff for certain parameter values, however within the expected range of variables the solver employed did not make a significant difference. Using the MATLAB inbuilt function `ode45`, an explicit Runge-Kutta method with Dormand-Prince coefficients, the sensitivity of the system to parameters of surface tension, viscosity, temperature, and growth rate was evaluated and plotted to show the relative impact of each one. With little known about exact values for the solution, these parameters were estimated within a reasonable tolerance from knowledge of other similar materials and the pure elements, though it was found that surface tension and molar flow rate had the most influence on bubble growth.

With the model developed, it was then applied to experimental data recorded by Wainwright et al. (2019). Growth events were found in footage recorded with a high speed camera focused on a scintillator board that picked up images of the burning Al:Zr particles from x-ray beams with phase contrast imaging. The footage was recorded at 90,000 fps with a spatial resolution of 2 µm per pixel and a total area of 768 µm $\times$ 768 µm. Despite the high frame rate, the number of growth events observed that fit prior assumptions of the model and had a sufficient number of frames showing the bubble was limited to three occurrences. Of these events, two were of

rapid growth that resulted in microexplosions and the other was slow growth to a hollow shelled particle. The bubble radius was plotted for each event per frame along with a simulation from the model for each of the proposed schemes for molar flow into the bubble. Within limits of uncertainty on the measurements, it was found that the molar flow scheme that was first order proportional to bubble radius had the best agreement with the data and so was selected as the representative expression for nitrogen in the bubble. While parameter values for growth rate and nucleation time were found using trial and error, further analysis showed that changing other variables in the system would counter any error presented by using a wrong value.

The system was then modelled in two dimensions using COMSOL Multiphysics. Solutions of a 2D axisymmetric component with the laminar flow module and a moving mesh were consistent with those from the one dimension case, though with a discrepancy caused by changing the initial conditions which was expected for the nonlinear governing equations. Additionally, the 2D model was simulated for a range of offset bubble nucleations which found that bubble growth was not affected, but convergence started to fail sooner as the liquid phase was compressed on the near side of the nucleation. With the moving mesh, this compression caused the mesh to become heavily skewed, though this may also indicate that the droplet was about to burst as the liquid phase became too thin. While it was thought that the bubble would migrate to the centre of the droplet it was found to be negligible, especially when compared to the difference between the top and bottom of the liquid phase.

Finally the concentration of nitrogen in liquid phase was modelled using Fick's second law to see how the growth of the bubble affects the concentration profile. The PDE was solved using the Crank-Nicolson method for a number of different boundary conditions, with a coordinate transform coupling it with the bubble growth ODE. From these conditions, the two where flux is dependent on the concentration were not in agreement with the event analysis. Instead by applying a Neumann condition where the flux is explicitly defined as linearly proportional to radius, the minimum concentration required to fit the event was found to be around 0.3% of the initial atomic make up in the droplet. While the solubility of nitrogen in the liquid metal composite is unknown, this value appears reasonable as it is around 0.07 wt.% which is lower than levels observed in other liquid metals.

Further study into the topic could focus on finding an expression for flux at the boundary that depends on concentration and fits with the experimental results. With the current boundary conditions, the only factors considered were of concentration at the interface and in the bubble, though it is possible that flux may be determined by a more complex equation based on adsorption rates. Another aspect to look into further is the use of gradient descent algorithms to better obtain parameter values that minimise residual errors between data points and the solution. This would provide a more thorough method for determining unknowns that could allow for

precise values for different variables given enough data from footage and known fluid properties, though this would require improved experiments that could increase both temporal and spatial resolutions. Ultimately, the work presented in this thesis provides new insights toward understanding dynamics and chemical transport in burning metal droplets. From this point, there is the possibility of continuing this work in order to predict the probability of given particles undergoing microexplosion, and allow for the designing of new composite powders that optimise burn characteristics for individual applications.

Bibliography

D. Barthès-Biesel and A. Acrivos. Deformation and burst of a liquid droplet freely suspended in a linear shear field. *Journal of Fluid Mechanics*, 61(1):1–22, 1973. ISSN 14697645. doi: 10.1017/S0022112073000534. URL https://doi.org/10.1017/S0022112073000534.

N. Bremond and E. Villermaux. Bursting thin liquid films. *Journal of Fluid Mechanics*, 524:121–130, 2005. ISSN 00221120. doi: 10.1017/S0022112004002411. URL https://doi.org/10.1017/S0022112004002411.

J. C. Butcher. *The Numerical Analysis of Ordinary Differential Equations: Runge-Kutta and General Linear Methods*. Wiley-Interscience, USA, 1987. ISBN 0471910465.

Jixin Chen. Stochastic Adsorption of Diluted Solute Molecules at Interfaces. 2020.

A. T. Dinsdale and P. N. Quested. The viscosity of aluminium and its alloys - A review of data and models. In *Journal of Materials Science*, volume 39, pages 7221–7228. Springer, 2004. doi: 10.1023/B:JMSC.0000048735.50256.96. URL https://link.springer.com/article/10.1023/B:JMSC.0000048735.50256.96.

I. Egry, E. Ricci, R. Novakovic, and S. Ozawa. Surface tension of liquid metals and alloys-Recent developments, 2010. ISSN 00018686.

James J. Feng and Christopher A. Bertelo. Prediction of bubble growth and size distribution in polymer foaming based on a new heterogeneous nucleation model. *Journal of Rheology*, 48(2):439–462, 2004. ISSN 0148-6055. doi: 10.1122/1.1645518.

Michio Inouye, Yasushi Kojima, Takao Choh, Seita Uekawa, and Yukinaga Yamada. On the Measurements of Diffusion Coefficients of Nitrogen in the Liquid Iron. *Tetsu-to-Hagane*, 59(2):205–213, feb 1973. ISSN 0021-1575. doi: 10.2355/tetsutohagane1955.59.2_205. URL https://www.jstage.jst.go.jp/article/tetsutohagane1955/59/2/59_2_205/_article/-char/ja/.

R. G. Kirk and E. J. Gunter. Transient Journal Bearing Analysis. *NASA Contractor Reports*, 1970. ISSN 05657059.

Lu Liu, Wenjing Ma, Mo Wang, and Luxiang Zong. Comparison of bubble growth process within a superheated water droplet and in superheated water due to rapid depressurization. *International Journal of Heat and Mass Transfer*, 109:659–667, 2017. ISSN 00179310. doi: 10.1016/j.ijheatmasstransfer.2017.02.031. URL https://www.sciencedirect.com/science/article/pii/S0017931016330253.

K. C. Mills and Y. C. Su. Review of surface tension data for metallic elements and alloys: Part 1 - Pure metals, 2006. ISSN 09506608.

Min-Kyu Paek, Jung-Mock Jang, Kyung-Hyo Do, and Jong-Jin Pak. Nitrogen Solubility in High Manganese-Aluminum Alloyed Liquid Steels. *Met. Mater. Int*, 19(5): 1077–1081, 2013. doi: 10.1007/s12540-013-5024-0.

P. F. Paradis, T. Ishikawa, and S. Yoda. Non-Contact Measurements of Surface Tension and Viscosity of Niobium, Zirconium, and Titanium Using an Electrostatic Levitation Furnace. *International Journal of Thermophysics*, 2002. ISSN 0195928X. doi: 10.1023/A:1015459222027.

E. M. Sacris and N. A.D. Parlee. The diffusion of hydrogen in liquid Ni, Cu, Ag, and Sn. Technical Report 12, 1970.

S. S. Sazhin, O. Rybdylova, C. Crua, M. Heikal, M. A. Ismael, Z. Nissar, and A. Rashid B.A. Aziz. A simple model for puffing/micro-explosions in water-fuel emulsion droplets. *International Journal of Heat and Mass Transfer*, pages 815–821, 2019. ISSN 00179310. doi: 10.1016/j.ijheatmasstransfer.2018.11.065. URL `https://doi.org/10.1016/j.ijheatmasstransfer.2018.11.065`.

Johannes Schindelin, Ignacio Arganda-Carreras, Erwin Frise, Verena Kaynig, Mark Longair, Tobias Pietzsch, Stephan Preibisch, Curtis Rueden, Stephan Saalfeld, Benjamin Schmid, Jean Yves Tinevez, Daniel James White, Volker Hartenstein, Kevin Eliceiri, Pavel Tomancak, and Albert Cardona. Fiji: An open-source platform for biological-image analysis. *Nature Methods*, 9(7):676–682, 2012. ISSN 15487091. doi: 10.1038/nmeth.2019. URL `http://fiji.sc/Adding{_}Update{_}Sites`.

J. Shinjo, J. Xia, L. C. Ganippa, and A. Megaritis. Physics of puffing and microexplosion of emulsion fuel droplets. *Physics of Fluids*, 26(10), 2014. ISSN 10897666. doi: 10.1063/1.4897918.

J. Shinjo, J. Xia, L. C. Ganippa, and A. Megaritis. Puffing-enhanced fuel/air mixing of an evaporating n-decane/ethanol emulsion droplet and a droplet group under convective heating. *Journal of Fluid Mechanics*, 793:444–476, 2016. ISSN 14697645. doi: 10.1017/jfm.2016.130. URL `https://doi.org/10.1017/jfm.2016.130`.

Endre Süli and David F Mayers. *An Introduction to Numerical Analysis*. Cambridge University Press, 2003. ISBN 9780521810265. URL `www.cambridge.org/9780521810265`.

William Thielicke. *The flapping flight of birds: Analysis and application*. PhD thesis, University of Groningen, 2014.

Elliot R. Wainwright, Travis A. Schmauss, Shashank Vummidi Lakshman, Kyle R. Overdeep, and Timothy P. Weihs. Observations during Al:Zr composite particle combustion in varied gas environments. *Combustion and Flame*, 196:487–499, 2018. ISSN 15562921. doi: 10.1016/j.combustflame.2018.06.026.

Elliot R. Wainwright, Shashank V. Lakshman, Andrew F.T. Leong, Alex H. Kinsey, John D. Gibbins, Shane Q. Arlington, Tao Sun, Kamel Fezzaa, Todd C. Hufnagel, and Timothy P. Weihs. Viewing internal bubbling and microexplosions in combusting metal particles via x-ray phase contrast imaging. *Combustion and Flame*, 199:194–203, 2019. ISSN 15562921. doi: 10.1016/j.combustflame.2018.10.019. URL `https://www.sciencedirect.com/science/article/pii/S0010218018304462`.

Shiping Wang, Wenyang Duan, and Qianxi Wang. The bursting of a toroidal bubble at a free surface. *Ocean Engineering*, 109:611–622, 2015. ISSN 00298018. doi: 10.1016/j.oceaneng.2015.09.017.

Jun Xia and Junji Shinjo. Microexplosion and Puffing of an Emulsion Fuel Droplet. 2017. doi: 10.4995/ilass2017.2017.4762. URL `http://dx.doi.org/10.4995/ILASS2017.2017.4762`.

Qian Qian Yang, Yuan Liu, and Yan Xiang Li. Hydrogen diffusion coefficient in liquid metals evaluated by solid-gas eutectic unidirectional solidification. *Transactions of Nonferrous Metals Society of China (English Edition)*, 24(12):4030–4037, dec 2014. ISSN 10036326. doi: 10.1016/S1003-6326(14)63565-2.